Materials Today Bio 27 (2024) 101150

Contents lists available at ScienceDirect

Materials Today Bio

journal homepage: www.journals.elsevier.com/materials-today-bio

Enhanced vascularization and osseointegration under osteoporotic conditions through functional peptide coating on implant surfaces

Jiming Liu [a,1], Bingyang Zhao [b,1], Xinkun Shen [c], Dandan Lu [a], Wei he [a], Xingjie Zan [d], Lianxin Li [e,*], Yihuai Pan [a,**]

[a] School & Hospital of Stomatology, Wenzhou Medical University, Wenzhou, 325000, China
[b] The Department of Stomatology, The First Affiliated Hospital of Ningbo University, Ningbo, 315010, China
[c] Department of Orthopaedics, The Third Affiliated Hospital of Wenzhou Medical University (Ruian People's Hospital), Wenzhou, 325016, China
[d] Wenzhou Key Laboratory of Perioperative Medicine, Wenzhou Institute, University of Chinese Academy of Sciences, Wenzhou, 325000, China
[e] Department of Orthopaedics Surgery, Shandong Provincial Hospital Affiliated to Shandong First Medical University, Jinan City, Shandong Province, 250021, China

ARTICLE INFO

Keywords:
Osseointegration
Multifunctional coatings
Osteoporotic bone defects
Vascularization
Bone regeneration

ABSTRACT

Patients with osteoporosis face challenges such as decreased bone density, a sparse trabecular structure, weakened osteogenic ability, and impaired angiogenesis, leading to poor osseointegration and implant failure. Surface modification of implants with biologically active molecules possessing various functions is an effective strategy to improve osseointegration. In this study, we constructed a simple multifunctional coating interface that significantly improves osseointegration. In brief, a multifunctional coating interface was constructed by coupling the Rgd adhesive peptide, Ogp osteogenic peptide, and Ang angiogenic peptide to Lys_6 (k_6), which self-assembled layer by layer with TA to form the (TA-Rgd@ogp@ang)n composite membrane. This study characterized the surface morphology and biomechanical properties of the coating under both gas and liquid phases and monitored the deposition process and reaction rate of the two peptides with TA using a quartz crystal microbalance. Moreover, (TA-Rgd@ogp@ang)n exhibited a triple synergistic effect on cell migration and adhesion, osteogenic differentiation, and angiogenesis. It also ameliorated the high ROS environment characteristic of osteoporosis pathology, promoted angiogenic bone defect regeneration in osteoporosis, thereby avoiding poor osseointegration. This work provides a new approach for the prevention of implant failure in pathological environments by constructing multifunctional coatings on implants, with tremendous potential applications in the fields of orthopedics and dentistry.

1. Introduction

The efficient osseointegration at the interface between bone and implant is a dynamic process, wherein cells surrounding the implant secrete various cellular factors to promote the recruitment of osteogenic cells and induce osteogenic differentiation, thereby establishing a direct and stable connection between bone and implant to achieve osseous integration [1–3]. This process plays a crucial role in the successful placement of intraosseous implants in clinical practice. Osteoporosis is a chronic metabolic disease prevalent worldwide, particularly among postmenopausal women and individuals aged 50 and above [4,5], who also constitute a significant population requiring dental implants. However, osteoporosis is characterized by abnormal osteoclast activity and impaired osteogenic potential of bone marrow mesenchymal stem cells, leading to an imbalance in bone homeostasis, manifested clinically as decreased bone density, alterations in trabecular bone structure, and prolonged bone healing time [6,7]. Compared to normal bone, osteoporotic bone exhibits a diminished capacity for recruiting mesenchymal stem cells and osteogenic cells, shows limited osteogenic function, excessive osteoclastic resorption, and impaired angiogenesis during the bone integration process, resulting in implant failure [8–10]. Therefore, achieving osseointegration of implants under osteoporotic pathological conditions presents a significant challenge.

Natural titanium and its alloys are widely used in the field of

* Corresponding author.
** Corresponding author.
E-mail addresses: 13505312449@163.com (L. Li), yihuaipan@wmu.edu.cn (Y. Pan).
[1] These authors contributed equally to this work.

https://doi.org/10.1016/j.mtbio.2024.101150
Received 21 April 2024; Received in revised form 13 June 2024; Accepted 7 July 2024
Available online 14 July 2024

orthopedics due to their excellent biocompatibility, corrosion resistance, lightweight, and superior mechanical properties [11]. However, the inherent biological inertness of bare titanium implants weakens bone integration [12]. For patients with metabolic diseases such as osteoporosis, these bare implants are more prone to failure. Various surface modification strategies to promote osseointegration on titanium surfaces have been extensively researched, which include doping of inorganic coatings, immobilization of bioactive molecules, and layer-by-layer assembly techniques. Among them, the fixation of fusion peptides (FPs) via silanization presents a promising approach as it can simultaneously address multiple biological behaviors, effectively overcoming the challenge of limited anchoring sites in achieving multifunctional biological processes [13,14]. The research team led by Yong Huang first modified the Ti surface with alkynyl-functionalized silane reagents in a one-step manner, and then linearly fused antimicrobial peptides (AMPs, HHC36) and osteogenic peptides (Rgd) via orthogonal click reactions. This peptide-modified titanium (Ti) implant coating possesses dual functionality of antimicrobial and osteogenic promotion, effectively promoting osseointegration [15]. However, silanization is highly dependent on the metal substrate and may not be a universally applicable fixation method. As titanium metal gradually replaces other materials, this modification approach may lose its original advantages. Yong Huang's team further combined the fusion peptide-modified titanium dioxide nanotubes with 3D printed titanium scaffolds to create a new dual-functional scaffold with bone induction and antibacterial properties [16]. However, when fusion peptide chains are too long, it may cause misalignment or loss of amino acid sequences, and maintaining the respective conformations of two peptide domains close to each other may affect their functionality. Inspired by mussels, dopamine (DOPA) is another widely used method for connecting surfaces with biomolecules. Bai et al. conjugated bone marrow mesenchymal stem cell (BMSC)-targeting peptide sequence (E7) and osteogenic growth peptide (Y5) with DOPA to achieve cell settlement and osteogenic differentiation on the implant surface [17]. However, this method fails to explain the quantity and proportion of the two peptides on the interface, and the presentation of peptide bases at the material interface is elusive. Layer-by-layer assembly (LbL) is a universal surface technique, and its assembly process is gentle, making it more suitable for bioactive coatings [18,19]. However, traditional LbL requires assembly units such as polymers, and active biological molecules may be easily buried beneath the modification layer, rendering them unable to express [20]. Existing reports have made substantial progress in constructing multifunctional implant interfaces, but overcoming these challenges and improving the efficiency and reliability of peptide-modified materials remains a significant challenge.

Tannic acid (TA) is a natural polyphenol derived from plants and is rich in phenolic hydroxyl groups. It offers abundant reactive sites and is easily complexed with various types of peptides, leading to the development of diverse functional materials for various applications and plays a crucial role in bone tissue engineering [21–23]. In a previous study by our research group, we constructed a functional platform based on polyamino acids and short peptides. Through a polyphenol-peptide network, LbL techniques were employed, where polyamino acid linkers and polyphenols were sequentially assembled through electrostatic interactions [24]. Multiple short peptides with different functionalities could form multilayer composite films at the interface through common polyamino acid linkers. This assembly method addresses issues such as burst release observed in previous studies while preserving the original structures and functionalities of individual peptides. This provides new insights into meeting the diverse requirements for bone integration in osteoporosis.

Based on the pathological characteristics of osteoporosis, an ideal implant for the treatment of osteoporotic bone defects should possess multiple functions, such as the ability to regulate the surrounding pathological microenvironment for bone homeostasis, strong stem cell migration and adhesion capabilities, and promotion of osteogenesis and angiogenesis. Peptides exhibit rich functionality in this regard. Among them, the Rgd adhesion peptide (arginine-glycine-aspartic acid) interacts extensively with cell membrane integrins, guiding cell adhesion and migration [25]. Ogp is a physiologically endogenous fourteen-amino acid peptide found in human serum, capable of promoting the differentiation of bone marrow stem cells into osteoblasts [26,27]. A novel binding sequence, Ser-Val-Val-Tyr-Gly-Leu-Arg (SVVYGLR), has been identified as an amino acid sequence in osteopontin (OPN) involved in angiogenesis [28]. The vascular system is essential for the transport of nutrients, oxygen, hormones, growth factors, and neurotransmitters and is indispensable for osteogenesis. The SVVYGLR peptide significantly promotes the adhesion and proliferation of BMSCs and possesses the multiple functions, such as inhibiting osteoclast growth, enhancing osteoblast proliferation and differentiation, and promoting vascularized bone regeneration and remodeling [29].

Therefore, in this study, leveraging the aforementioned platform concept, we utilized the common hexamer lysine K_6 to simultaneously integrate the Rgd adhesion peptide, which possesses cell migration and adhesion capabilities; the Ogp peptide, which promotes stem cell and osteogenic differentiation; and the SVVYGLR peptide, which exhibits angiogenic osteogenic properties (referred to as the angiogenic peptide Ang in this paper), into a composite membrane, termed (TA-Rgd@ogp@ang)n. This composite membrane aims to improve osseointegration of implants and regulate bone homeostasis under osteoporotic conditions (Scheme 1). The paper analyzes the deposition process, physicochemical properties, mechanical performance, and visualization of peptide fixation of the (TA-Rgd@ogp@ang)n membrane. Additionally, the (TA-Rgd@ogp@ang)n membrane effectively promoted early cell migration and adhesion, ameliorated the high ROS environment in osteoporosis, induced osteogenic differentiation and mineralization of osteoblast precursor cells and bone marrow mesenchymal stem cells (BMSCs), and promoted vascularized bone regeneration. This represents a novel and effective strategy for improving osseointegration of implants under osteoporotic conditions.

2. Materials and methods

2.1. Materials

TA (molecular weight, 1701.2 Da), Ogp (KKKKKK-GGYGFG-GYGFGG), Rgd (KKKKKK-Acp-Rgd-Acp-Rgd-Acp), and Ang (KKKKKK-Acp-SVVYGLRSVVYGLR) polypeptides were synthesized by Nanjing Peptide Valley Biotechnology Co., Ltd (Nanjing, China), 30 % hydrogen peroxide (H_2O_2), 25 % ammonia, 98 % sulfuric acid, tris (hydroxymethyl)-aminomethane (Tris) (≥99 %), Actin Fluorescent Myosin, Triton X-100, Paraformaldehyde (4 %), sodium β-glycerophosphate, alizarin red S, and fetal bovine serum (FBS) were purchased from Gibco. Vitamin C, BCIP/NBT alkaline phosphatase kit, 4,6-diamidino2-phenylindole (DAPI) and Counting Kit-8 (CCK-8) were purchased from Beyotime Institute of Biotechnology. Matrix gel, Immunofluorescence staining of CD31.Silicon wafers and 14-mmdiameter round glass coverslips were washed at 98 °C with piranha solution (30 % hydrogen peroxide and 70 % concentrated sulfuric acid, V/V) for 2 h, followed by repeated washing with anhydrous ethanol and deionized water under sonication, and dried under nitrogen airffow.

2.2. Preparation of the(TA-Rgd)n, (TA-Rgd@ogp)n, (TA-Ogp@ang)n, (TA-Rgd@ang)n, and (TA-Rgd@ogp@ang)n coating

First, freshly cut 1 cm × 1 cm silicon wafers were cleaned with piranha solution (a mixture of 70 % concentrated H_2SO_4 and 30 % H_2O_2) at 95 °C for 2 h, followed by thorough rinsing with deionized water and drying with a stream of dry nitrogen gas. The pretreated clean silicon wafers were used as substrates for coating deposition and layer-by-layer (LbL) assembly. Subsequently, TA, Rgd, Ogp, and Ang were separately dissolved in buffer solutions at a concentration of 1 mg/mL at pH 7. The

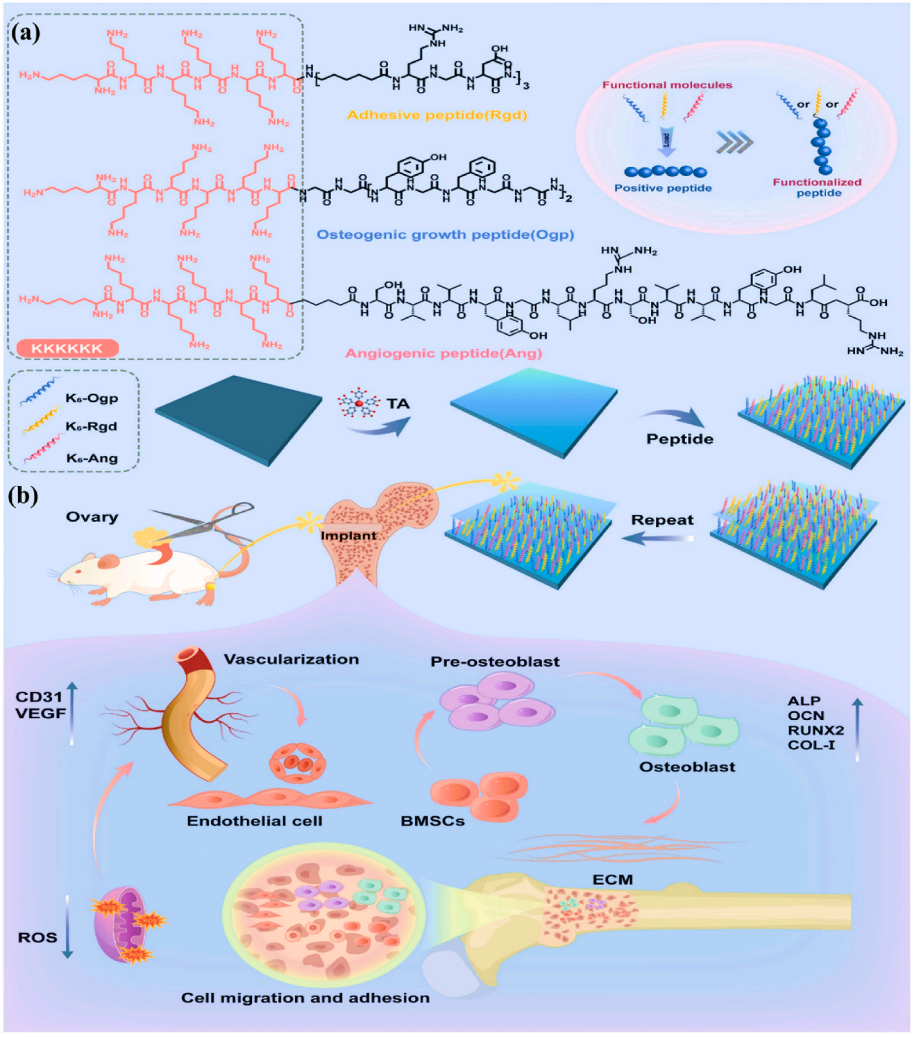

Scheme 1. (a) The amino-acid structural formula of the polypeptide. (b) Coating preparation process and biological applications.

buffer solution used was 10 mM Tris-HCl, pH adjusted to 7 using 1 M Tris or HCl. The three peptides were combined pairwise in proportion to form new solutions [22] (in accordance with previous studies, based on mass ratios), resulting in Rgd@ogp, Ogp@ang, Rgd@ang, and Rgd@ogp@ang, each at a total concentration of 1 mg/mL (pH = 7). The substrates were alternately immersed in TA and peptide solutions, with each single-layer immersion lasting for 10 min, until the desired number of layers (n) was obtained. After each layer immersion, thorough rinsing with deionized water and drying with nitrogen gas were performed, resulting in (TA-Rgd)n, (TA-Rgd@ogp)n, (TA-Ogp@ang)n, (TA-Rgd@ang)n, and (TA-Rgd@ogp@ang)n coatings.

2.3. Thickness test of coating

The ellipsometric spectroscopy model (SE) can accurately monitor the changes in polarization state of incident light waves at material interfaces upon reflection by measuring the polarizing angle (ψ) and phase difference (Δ) , and also can calculate the refractive index, thickness, and quality of the information interface coating. The Woollam M2000UI ellipsometric spectrometer (J.A. Woollam Co., Inc., Lincoln, NE) was utilized, with WVASE32 serving as the analysis software, employing two incident angles, 65° and 70°. The values of ψ (polarization angle) and Δ (phase) were measured between 245 and 1000 nm. These two parameters (ψ and Δ) are related to the thickness and optical properties of the sample and can be calculated using the following equations:

$$tan\,\psi e^{i\Delta} \equiv \frac{r_p}{r_s} \equiv \rho\left(\theta_0, h_1, \ldots, h_j, N_a, N_S, N_1, \ldots., N_J\right)$$

where rp and rs are the reflection coefficients parallel and perpendicular to the incident surface, respectively, ρ is the complex reflectance, θ0 is the angle of incidence, hj is the thickness of the layer, and Na, Ns, and Nj are the complex refractive indices of the environment, substrate, and layer, respectively.

2.4. Quartz crystal microbalance

The dynamics of film assembly during the layer-by-layer process were monitored using a quartz crystal microbalance with dissipation monitoring (QCM-D) capable of dissipative functionality. Gold-coated quartz crystal sensors were cleaned in a mixture of $NH_3{\cdot}H_2O$ (25 %), H_2O_2 (30 %), and H_2O (1:1:5) at 75 °C for 1 h, followed by thorough rinsing with deionized water and drying with nitrogen gas. The gold-coated quartz crystal sensors were then installed in the flow chamber of a Q-Sense instrument, and Tris-HCl buffer solution was flowed over the chip until the system reached equilibrium. Subsequently, TA, buffer solution, peptides, and buffer solution were sequentially passed through the chip, each for 10 min, until the desired number of layers (n) was achieved. The flow rate of the injected solution was 100 μL/min, and real-time monitoring of changes in energy dissipation (ΔD) and resonance frequency (Δf) at different harmonics (ν = 3, 5, 7, 9 …) was performed. Data from ν = 3 were used for image plotting.

2.5. X-ray photoelectron spectrometer analysis

The assembled TA/peptide coatings were characterized using X-ray photoelectron spectroscopy (ESCALAB 250) to obtain peak data under the conditions of a take-off angle of 90° and an energy of 20 eV. For the subsequent material characterization experiments, the experimental groups are (TA-Rgd)n, (TA-Rgd @ ogp)n, (TA-Ogp @ ang)n, (TA-Rgd@ang)n, and (TA-Rgd @ ogp @ ang)n, with n = 10.

2.6. Water contact angle characterization of coatings

The contact angle is the angle between the solid-liquid interface passing through the liquid interior and the gas-liquid interface. In research, the water contact angle (WCA) is commonly used to measure the hydrophilicity of materials. This experiment uses the static contact angle drop method using the KRUSS DSA1 1.80 version contact angle analyzer. Deionized water was used as the probing droplet to measure the WCA of the samples. Specifically, 5 μL of ultrapure water was precisely dropped onto the sample surface, and the moment of contact between the ultrapure water and the sample surface was captured using a high-speed camera. Then use OneAttension software to analyze the size of the WCA. Water contact angle need to be measured at least 3 time with 6 spots on one sample.

2.7. Coating stability test

The prepared TA/polypeptide coating was immersed in PBS buffer, and the film thickness was measured at 1, 2, 3, and 4 weeks. The stability of the coating was explained by the change of film thickness with immersion time.

2.8. Mechanical performance testing of coatings

Surface mechanical properties, morphology, adhesion, and roughness of the coatings were measured using an atomic force microscope (AFM, Dimension Icon, Bruker). Firstly, the samples were placed on the AFM sample stage and securely fixed using vacuum adsorption. Subsequently, the surface of the coating samples was characterized using the tapping mode of MikroMash silicon cantilevers, and roughness was calculated using accompanying software. To calculate the Young's modulus, the Derjaguin-Muller-Toporov model was employed to fit the retraction curves of force versus separation obtained from the AFM measurements. The principle of adhesion energy testing involves applying appropriate force to the coating using an AFM probe. As the probe approaches the coating, it experiences attractive forces. Upon contact with the coating, these attractive forces transform into repulsive forces, and the measured force corresponds to the adhesion energy of the coating.

2.9. SEM testing of coatings

By utilizing SEM (Scanning Electron Microscope), we observe and analyze the surface morphology and microstructure of coatings. In the SEM testing process, the coating samples first need to be properly prepared to ensure good conductivity and cleanliness. Then, the samples are placed in the scanning electron microscope, where signals (such as secondary electrons) generated by the interaction between high-energy electron beams and the coating surface are utilized to form images. By adjusting the parameters of the electron beam and applying image processing techniques, clear and detailed images of the coating surface morphology can be obtained.

2.10. Quantitative determination of polypeptides by fluorescence labeling

Visualization and quantitative determination of peptides were performed using fluorescence labeling. MCA-labeled Rgd, TAMRA-labeled Ogp, and FITC-labeled Ang were prepared to visualize the adsorption of the two peptides on the substrate surface. According to the previously mentioned coating preparation method, TA/peptides were assembled layer by layer into composite films (TA-Rgd)n, (TA-Rgd@ogp)n, (TA-Ogp@ang)n, (TA-Rgd@ang)n, and (TA-Rgd@ogp@ang)n, with n = 10. Subsequently, fluorescence distribution before and after assembly was monitored using laser confocal microscopy to determine peptide distribution, and fluorescence intensity was fitted using ImageJ software. Next, standard curves for the three fluorescently labeled peptides were obtained using a UV–visible near-infrared spectrophotometer. Finally, the absorption of residual fluorescent peptides in the solution before and after assembly was measured, and the peptides adsorbed on different combination interfaces were quantified using the standard curves.

2.11. Cell culture

This study involved three cell lines. MC3T3-E1 osteoblasts and bone marrow mesenchymal stem cells (BMSCs) derived from mouse bone marrow were obtained from Procell Life Science & Technology Co., Ltd. They were cultured at 37 °C in a 5 % carbon dioxide atmosphere in α-MEM basal medium supplemented with 100 U/mL penicillin, 100 mg/mL streptomycin, and 10 % FBS. Human umbilical vein endothelial cells (HUVECs) obtained from Procell Life Science & Technology Co., Ltd. were cultured at 37 °C in a 5 % carbon dioxide atmosphere in DMEM basal medium supplemented with 100 U/mL penicillin, 100 mg/mL streptomycin, and 10 % FBS. All cell experiment groups were the control group, the (TA-Rgd)n group, the (TA-Rgd @ ogp)n group, the (TA-Ogp @ ang)n group, the (TA-Rgd @ ang)n group, and the (TA-Rgd @ ogp @ ang)n group, with n = 10.

2.12. Intracellular reactive oxygen species (ros) clearance experiment

The MC3T3-E1 cells (4×10^4) were seeded onto the coverslips in the wells of a 24-well plate, with both blanks and peptide-coated coverslips. After 24 h of culture, negative and positive controls were established, with the positive group stimulated by replacing the normal culture medium with H_2O_2 (500 μM). After 10 h of stimulation, the intracellular ROS detector DCFH-DA probe was added, and the cells were incubated in the dark in the cell culture incubator for 25 min. Subsequently, the cells were fixed with 4 % paraformaldehyde for 15 min, followed by staining of the cell nuclei and cytoskeleton with DAPI and phalloidin-labeled rhodamine, respectively, for 15 min and 30 min. The fluorescence intensity of ROS before and after stimulation, as well as changes in cell morphology and quantity, were observed using laser confocal microscopy, and the clearance of ROS was quantified using Image J software for statistical analysis.

2.13. Cell migration

The MC3T3-E1/HUVEC cells (1×10^5) were seeded onto the coverslips in the wells of a 24-well plate. After 1–2 days of culture, when the cells had fully covered the entire coverslip, three evenly spaced perpendicular scratches were made on each coverslip using a sterile 200 μL pipette tip. Subsequently, the coverslips were washed once with PBS, and the culture medium was replaced with serum-free medium. The cells were then cultured for an additional 24 h. Cell migration to the scratched area was observed and photographed using an inverted fluorescence microscope. The migration area of cells on each coverslip was analyzed using Image J software.

2.14. Cell adhesion test

To evaluate cell adhesion strength, MC3T3-E1 cells (2.5×10^4) were seeded in 24-well plates, divided into blank group, positive control group, (TA-Rgd)n, (TA-Rgd@ogp)n, (TA-Ogp@ang)n, (TA-Rgd@ang)n, and (TA-Rgd@ogp@ang)n groups, with n = 10. Glass slides coated with

collagen solution were used as the positive control group. After cell seeding, the cells were cultured in a cell culture incubator for 12 h, followed by agitation at 150 rpm for 30 min on a horizontal shaker. Cell viability in each group was assessed using the CCK8 assay kit, indirectly indicating the adhesion of cells to the coating surface. Additionally, the cell cytoskeleton and nuclei were stained after exposure to shear force for observation.

2.15. Early cell adhesion and spreading

First, MC3T3-E1/HUVEC cells (4×10^4) were seeded onto blank and peptide-coated cell slides in a 24-well plate. After incubation for 2 and 4 h, the cells were fixed with 4 % paraformaldehyde for 15 min each. Subsequently, 0.1 % TritonX-100 was added for 5 min to open the cell membrane channels. The cells were then stained for the cytoskeleton using rhodamine-phalloidin (red) for 30 min. After staining, the cells were washed three times with PBS for 10 min each wash. Next, the cells were stained for nuclei with DAPI (blue) for 15 min. The cells were washed again three times with PBS for 10 min each wash. Finally, the slides were sealed with anti-fluorescence quenching agent, and changes in cell number and morphology were observed using confocal laser scanning microscopy (CLSM). Cell adhesion and spreading area were analyzed using Image J.

2.16. Cell viability and proliferation

MC3T3-E1/HUVEC cells (1×10^4) were seeded onto blank and peptide-coated cell slides in a 24-well plate. The culture medium was changed every 1–2 days, and cell viability was assessed at two time points using the CCK8 assay kit. On the 6th day, the cells were fixed with paraformaldehyde, stained with Calcein/PI live-dead staining kit, and visualized using CLSM to observe cell proliferation images.

2.17. Tube formation assay

The tube formation assay was conducted to assess the angiogenic ability of HUVECs in *vitro*. Initially, HUVECs were seeded at a density of 2×10^4 cells per well in both empty wells and wells coated with peptides in a 24-well plate and cultured for 48 h. Subsequently, 50 μL of basement membrane matrix was added to each well of a 96-well plate and allowed to gel. The cells from each well were then centrifuged and seeded onto the gel at a density of 5000 cells per well, with serum-free medium. After 6 h of incubation, tube-like structures were imaged using an inverted microscope. The length and number of tubes were quantified using Image J software.

2.18. Tube formation-related immunofluorescence staining

Initially, human umbilical vein endothelial cells (HUVECs) were seeded at a density of 4×10^4 cells per well in both empty wells and wells coated with peptides in a 24-well plate. After 2 days of culture, the cells were fixed with 4 % paraformaldehyde solution, washed with PBS, and treated with 0.2 % Triton X-100 (Solarbio, China) for 15 min at room temperature. Subsequently, the cells were incubated with PBS containing 5 % bovine serum albumin (BSA) for 1 h at room temperature to block non-specific binding of CD31. Following blocking, the cells were incubated with CD31 antibody overnight at 4 °C in the dark. After washing with PBS, the cells were stained with DAPI for 5 min to visualize the cell nuclei, and images were acquired using laser confocal microscopy. The fluorescence intensity of CD31 was quantified using Image J software.

2.19. Osteogenic staining analysis

Seeding MC3T3-E1 cells at a density of 2×10^4 cells per well. On both the 4th and 7th days, the cells were fixed with 4 % paraformaldehyde for 15 min. Subsequently, ALP activity was detected using the BCIP/NBT staining kit, and staining was observed using an upright microscope. On the 14th and 21st days, cells were stained with a 0.1 % solution of Alizarin Red S (pH 4.2) for 30 min. After fixation, cells were washed with PBS three times, air-dried, and mounted with neutral gum for observation. BMSCs were seeded following the same procedure, and ALP staining was performed on the 4th and 7th days, while ARS staining was conducted on the 7th and 14th days.

2.20. Osteogenic genes expression

Investigation of tube formation and osteogenic-related gene expression was conducted separately. BMSCs/HUVEC were seeded at a density of 2×10^5 cells per well onto both blank and peptide-coated surfaces (peptide-coating was performed on cell slides in six-well plates). After 7 days of cell culture, total RNA from MC3T3-E1 cell samples was extracted using the FastPure® Cell/Tissue Total RNA Isolation Kit V2. The RNA was then reverse transcribed into cDNA using the HiScript III All-in-one RT SuperMix Perfect for qPCR kit. DNA samples were amplified using the Taq Pro Universal SYBR qPCR Master Mix kit. Finally, forward and reverse primers for osteogenic and tube formation-related genes, with β-actin serving as the housekeeping gene, are listed in Table S1. Data were analyzed using the $2^{-\triangle\triangle ct}$ method and normalized to the average of the control group.

2.21. Osteogenesis evaluation in vivo

The protocol for all animal implantation surgeries was approved by the Wenzhou Institute, University of Chinese Academy of Sciences. All procedures were conducted following the standards described in the guidelines for the care and use of laboratory animals. Ethics number: WIUCAS23061401.

2.21.1. Implantation surgery

Purchase 18 healthy female Sprague-Dawley rats, 10 weeks old, weighing 270–300g, from the Zhejiang Experimental Animal Center. Allow for a 1-week acclimatization period. Subsequently, establish the osteoporosis (OVX) model as follows: Prior to surgery, all animals are intraperitoneally anesthetized with a dose of 2 % sodium pentobarbital (Sigma Aldrich, USA) at 2 mL/kg body weight. A longitudinal incision is made on the right side of the spine, approximately 1 cm below the rib arch on the back. The skin, muscles, and peritoneum are sequentially incised to expose the bilateral ovaries (white fat masses), which are then thoroughly removed. Hemostasis is achieved by ligating bleeding points, followed by suturing. Three months later, Micro-CT testing is performed to confirm the successful establishment of the osteoporosis model, followed by bone implantation surgery.

The rats were randomly divided into 6 groups: Ti, (TA-Rgd)n, (TA-Rgd@ogp)n, (TA-Ogp@ang)n, (TA-Rgd@ang)n, and (TA-Rgd@ogp@ang)n, with $n = 10$. Each group consisted of 3 rats, totaling 6 titanium rods. During implantation, each rat received two implants with different surface modifications, with one implant inserted into each femur to minimize individual differences. Prior to surgery, all animals were intraperitoneally anesthetized with a dose of 2 % sodium pentobarbital at 2 mL/kg body weight, and the hind limbs were shaved. The rats were then positioned in a supine position and secured. Subsequently, a longitudinal incision was made at the midline of the knee joint skin, and the soft tissues were dissected. Using a dental handpiece, cylindrical holes with a diameter of 1.2 mm and a length of 10 mm were drilled along the longitudinal axis of the femur. The prepared titanium implants were then inserted into the holes. After surgery, the soft tissues were closed, and the skin was sutured. Eight weeks later, the rats were euthanized with an overdose of sodium pentobarbital, and the bilateral femurs were harvested and fixed in 4 % paraformaldehyde for subsequent testing.

2.21.2. Microcomputed tomography analysis

Micro-computed tomography (Micro-CT) was used to image the distal femur with the following parameters: voltage, 80 kV; current, 300 mA; scanning resolution of 18 μm. The specimen was rotated 360° at intervals of 0.5° during scanning. Following data acquisition and reconstruction, the proprietary software (CTAn and CTVol) was employed to reconstruct the region of interest around the distal femur and generate analyses of bone volume (BV), total volume of bone (TV), trabecular bone density, and trabecular separation.

2.21.3. Histology and histomorphometry

Histological analysis was performed to characterize the osseointegration at the bone-implant interface, primarily utilizing toluidine blue staining, HE staining, and Masson's trichrome staining. All samples were decalcified and embedded in paraffin, followed by tissue sectioning. Subsequently, the sections underwent staining with hematoxylin and eosin (HE), Masson's trichrome stain, and immunofluorescence staining for CD31/OCN.

2.22. Statistical analysis

All data are reported as the average of at least three duplicates, with the error bar indicating the standard deviation. At least 6 randomly selected images were performed to analyze cell numbers and cell area with Image J.Statistical analysis was performed using the *t*-test and one-way ANOVA, and significance was noted as * $p < 0.05$, ** $p < 0.01$, *** p

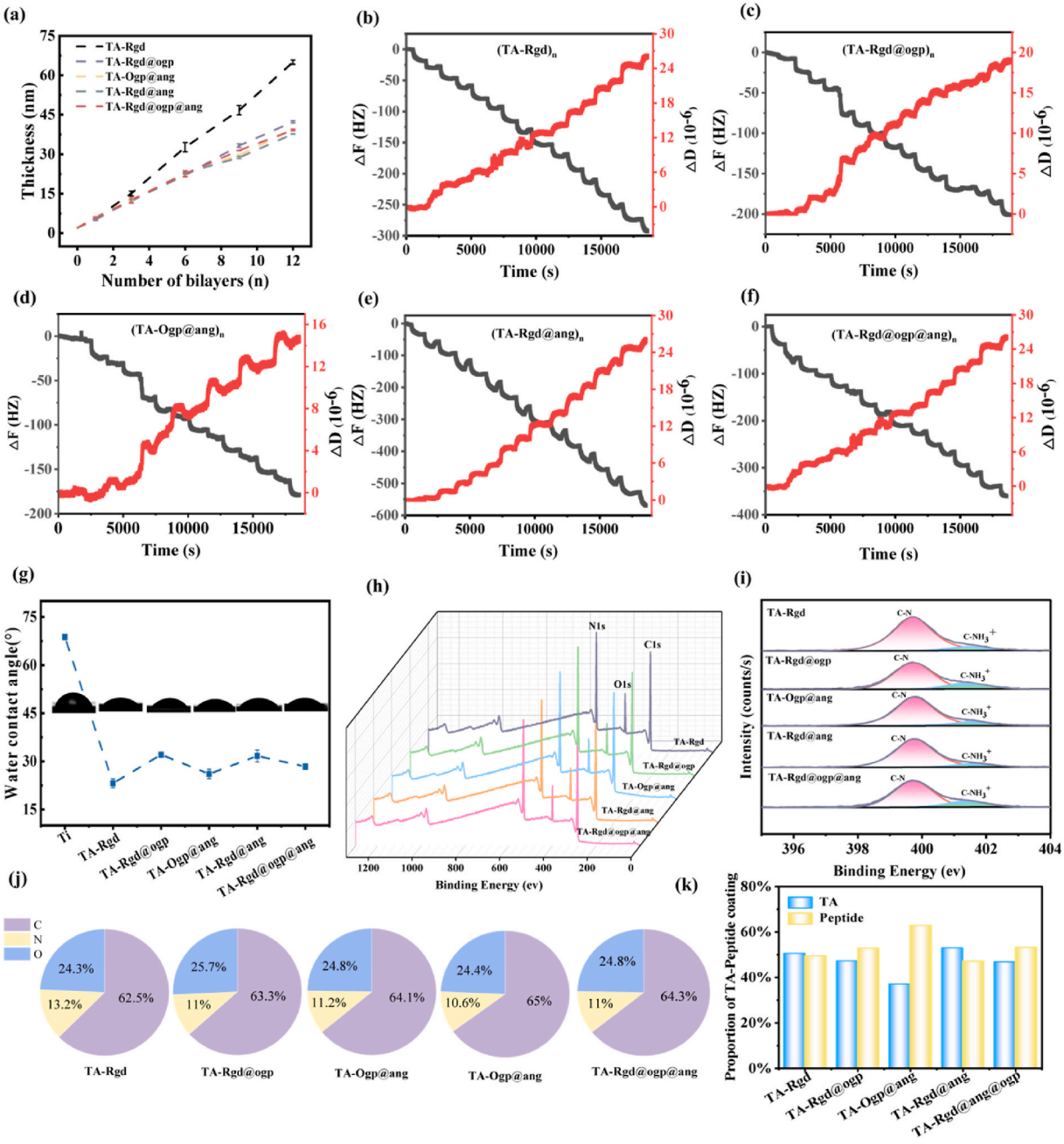

Fig. 1. (a) Thickness analysis of TA and different peptides at pH 7. (b–f) QCM-D analysis of TA and different peptides self-assembled deposition at pH 7 showing frequency and dissipation changes as functional curves of time. (g) Change of contact angle of TA-Rgd, TA-Rgd@Ogp, TA-Ogp@ang, TA-Rgd@ang and TA-Rgd@ogp@ang coatings. (h) XPS spectra of TA-Rgd, TA-Rgd@Ogp, TA-Ogp@ang, TA-Rgd@ang and TA-Rgd@ogp@ang coatings. (i) N1s spectra of TA-Rgd, TA-Rgd@Ogp, TA-Ogp@ang, TA-Rgd@ang and TA-Rgd@ogp@ang coatings. (j) Analyze element percentage content by XPS. (k) Composition analysis different coatings.

< 0.001, and $^{****}p < 0.0001$.

3. Result

3.1. Deposition process and material characterization of coatings

Firstly, according to the data from the ellipsometer (Fig. 1a), a trend of layer-by-layer growth is observed for TA and peptides at pH 7, indicating successful deposition of the coatings onto the substrate. Specifically, the TA-Rgd coating reached a thickness of 65 nm after assembly of 12 bilayers. Meanwhile, the thickness of coatings for TA-Rgd@ogp, TA-Ogp@ang, TA-Rgd@ang, and TA-Rgd@ogp@ang groups was relatively close, with deposition thickness ranging between 35 and 40 nm, significantly lower than that of the TA-Rgd coating. The deposition process of the self-assembled coatings was further monitored using quartz crystal microbalance with dissipation monitoring (QCM-D) (Fig. 1b–f). The frequency (f) of each group gradually decreased, indicating successful assembly of tannic acid and peptides on the substrate surface. Subsequently, by fitting the deposition curves with the Sauerbrey model, the adsorbed mass of TA and peptides in each layer of the thin films was obtained (Figs. S1a–b), along with the functional curves of deposition thickness and deposition layers. The total adsorbed mass of TA in the TA-Rgd coating was approximately 5256 ± 17.8 μm/cm^2, while the total adsorbed mass of peptides was 5516 ± 12.4 μm/cm^2. In the coatings of TA mixed with peptides from the other four groups, the adsorbed mass of both TA and peptides could reach 2500–3000 μm/cm^2. The deposition thickness data showed consistency with the ellipsometer results (Fig. S1c).

The surface properties of coatings can influence cellular behavior. This study investigated the hydrophilicity, stability, surface composition analysis, and mechanical properties of the coatings. Firstly, a smaller contact angle indicates better hydrophilicity of the material in water contact angle tests. As shown in Fig. 1g, the contact angles of the peptide-modified coatings decreased to 20–30° compared to pure titanium (68.8 ± 0.4°), with the lowest contact angle of 22.2 ± 1.4° observed for the TA-Rgd coating. These results indicate that the peptide-modified coatings significantly improve the hydrophilicity of pure titanium. Subsequently, stability tests of the coatings (Fig. S2) showed that after immersion in PBS for two weeks, the thickness decrease of the coatings was within 10 nm, the coating remains relatively stable within two weeks without significant release. Furthermore, XPS analysis was performed to further understand the proportion of compound composition and material interactions in the coating samples. Fig. 1h shows the complete spectra of the five peptide coatings, all containing nitrogen elements, indicating successful binding of peptides at the interface. **In Fig. 1i, peak deconvolution of the N peak reveals binding peaks of C–N and C–NH3+, without the presence of C=N bonds. Fig. 1j displays the atomic ratios on the TA-Rgd, TA-Rgd@ogp, TA-**

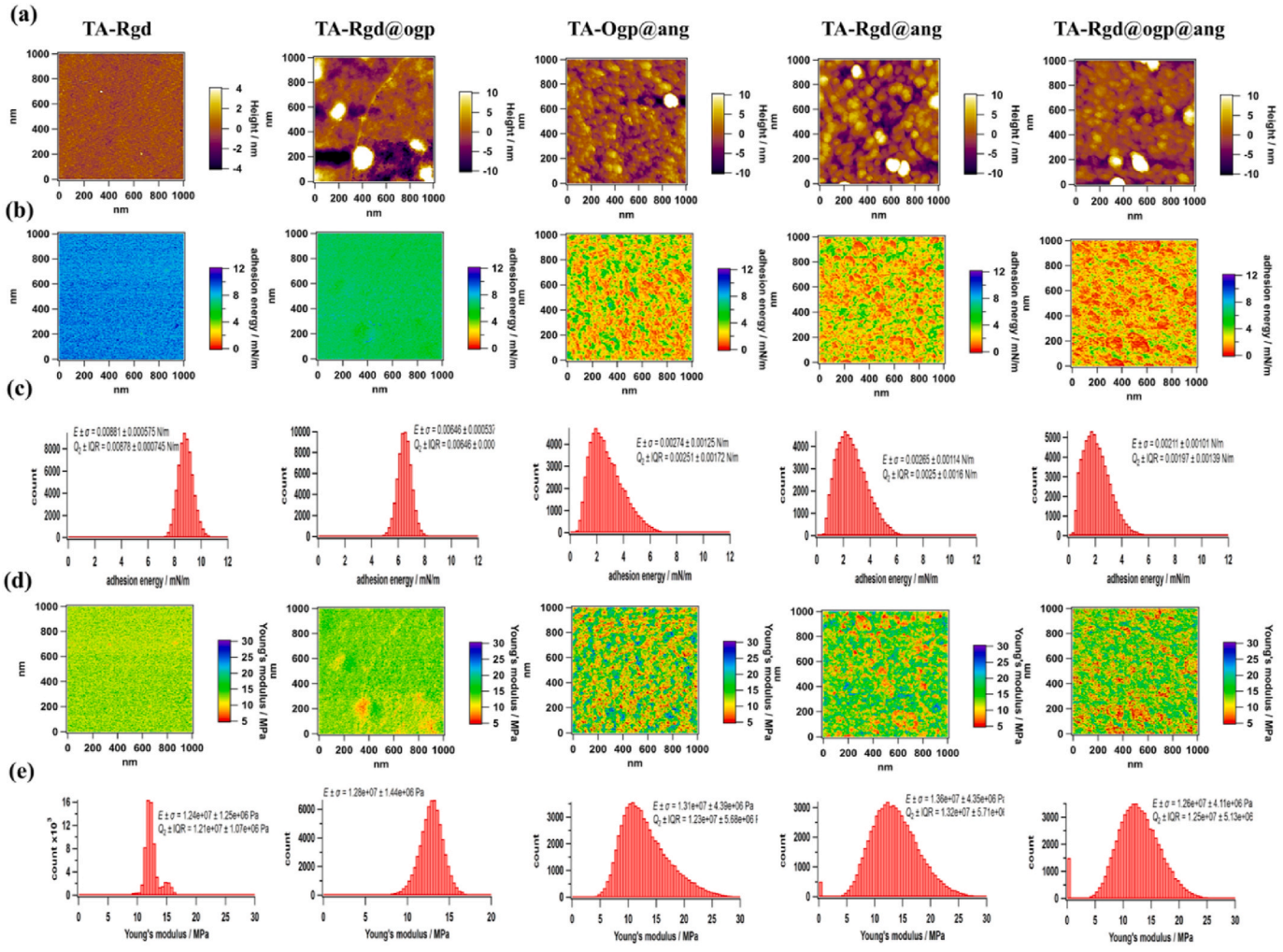

Fig. 2. (a) AFM images of TA-Rgd, TA-Rgd@Ogp, TA-Ogp@ang, TA-Rgd@ang and TA-Rgd@ogp@ang coatings in a liquid environment. (b) Adhesion energy images of TA-Rgd, TA-Rgd@Ogp, TA-Ogp@ang, TA-Rgd@ang and TA-Rgd@ogp@ang coatings in a liquid environment. (c) Gaussian distribution of the coating adhesion energy (d) Young's modulus images of TA-Rgd, TA-Rgd@Ogp, TA-Ogp@ang, TA-Rgd@ang and TA-Rgd@ogp@ang coatings in a liquid environment. (e) Gaussian distribution of the coated Young's modulus.

Ogp@ang, TA-Rgd@ang, and TA-Rgd@ogp@ang coatings, from which the molar mass ratio of TA to peptides on the five coatings was derived, as shown in Fig. 1k. Interestingly, except for the TA-Ogp@ang coating, the mass of TA is twice that of the peptides, while the mass ratio of TA to peptides on the other coatings is close to 1:1, similar to the feed ratio.

In AFM experiments, the surface morphology, mechanical properties, and adhesion energy of the interfaces of gas-phase (Fig. S3) and liquid-phase coatings (Fig. 2) were studied separately. In the gas phase, the surfaces of the TA-Rgd and TA-Rgd@ogp@ang coatings appeared uniformly smooth, while the morphologies of the TA-Rgd@ogp, TA-Ogp@ang, and TA-Rgd@ang coatings were similar, exhibiting discontinuous rough structures (Fig. S3a). As shown in Figs. S3b–c, the adhesion energy and Young's modulus of the coating surfaces followed a Gaussian distribution. Based on the JKR theory equation reflecting the adhesion force of the coatings, the surface adhesion energy of the peptide coatings was obtained, with the adhesion energy of the TA-Rgd coating being the highest at 0.0576 ± 0.00362 N/m, slightly lower for the other coating interfaces at 0.03–0.04 N/m. Figs. S3d–e showed that the Young's modulus of the TA-Rgd@ogp@ang ternary composite coating was the highest at 1.36 GPa. In the liquid phase, there were slight differences in morphology compared to the gas phase, with surfaces of all coatings except TA-Rgd exhibiting continuous spherical rough structures (Fig. 2a). The surface adhesion energy of the coatings remained highest for the TA-Rgd coating at 0.00881 ± 0.000575 N/m, approximately 10 times lower than in the gas phase (Fig. 2b–c). However, the Young's modulus decreased overall by three orders of magnitude, with the highest being 1.26 MPa for TA-Rgd@ang (Fig. 2d–e). As shown in Fig. S4, the microstructure of the coating surface can be observed under scanning electron microscopy (SEM).

3.2. Qualification of peptide content via fluorescent labeling

The above results confirm the binding of these peptides to the modified substrate surface; therefore, it is crucial to determine whether they are immobilized at the preset volume ratio. The fluorescence distribution at the coating interfaces of different experimental groups appears uniform (Fig. 3a). In samples treated with different ratios of mixed peptides, two and three peptides respectively exhibit distinct fluorescent labeling. Subsequently, quantitative analysis of the average fluorescence intensity and peptide density on different experimental groups was conducted (Fig. 3b and c), confirming that the trend of fluorescence intensity variation is consistent with the peptide ratio (Standard curves for polypeptide quantification are shown in Fig. S7). Interestingly, the amount of peptides adsorbed on the TA-Rgd coating is 54.9 μg, while the total amount adsorbed on both TA and mixed peptide coatings is close to 54.9 μg.

3.3. Oxidation resistance of the coating

To investigate the antioxidative properties of the coating interfaces, MC3T3-E1 cells were treated with a certain concentration of H_2O_2 to simulate the release of ROS in *vivo* under oxidative stress imbalance conditions. To observe the effects of H_2O_2 stimulation on cell status before and after, staining of the cell cytoskeleton and nucleus was performed (Figs. S5a–b). As shown in Fig. S5a, the morphology of H_2O_2-stimulated blank control cells exhibited shrinkage and elongation. In contrast, cells on the TA-Rgd, TA-Rgd@ogp, TA-Ogp@ang, TA-Rgd@ang, and TA-Rgd@ogp@ang membranes showed no obvious changes. The morphology of the blank control cells without H_2O_2 stimulation was normal and exhibited tight connections (Fig. S5b). Subsequently, statistical analysis of the changes in cell area for each group was conducted (Fig. S5c). It was observed that compared to cells before H_2O_2 treatment, the cell area of the control group (in red) significantly decreased, while the cell area on the membranes of the other groups showed no significant changes. Furthermore, changes in the immunofluorescence intensity of ROS fluorescence probes (in green) were analyzed to intuitively assess the ROS content inside the cells. As shown in Figs. S5a–b, the green fluorescence intensity of the four groups stimulated with H_2O_2 was significantly higher than that of the non-stimulated groups, indicating successful induction of ROS by the H_2O_2 model. After H_2O_2 stimulation, the ROS fluorescence intensity of cells on the TA-Rgd, TA-Rgd@ogp, TA-Ogp@ang, TA-Rgd@ang, and TA-Rgd@ogp@ang membranes decreased to varying degrees compared to the blank control. Quantitative analysis of the average fluorescence intensity of ROS produced by each group in Fig. S5d revealed that after H_2O_2 stimulation, the average fluorescence intensity on the blank surface reached 130 RFU, while the intensity on the membranes of the other five groups decreased to around 100 RFU. Therefore, it can be concluded that the coating surfaces have the ability to scavenge reactive oxygen

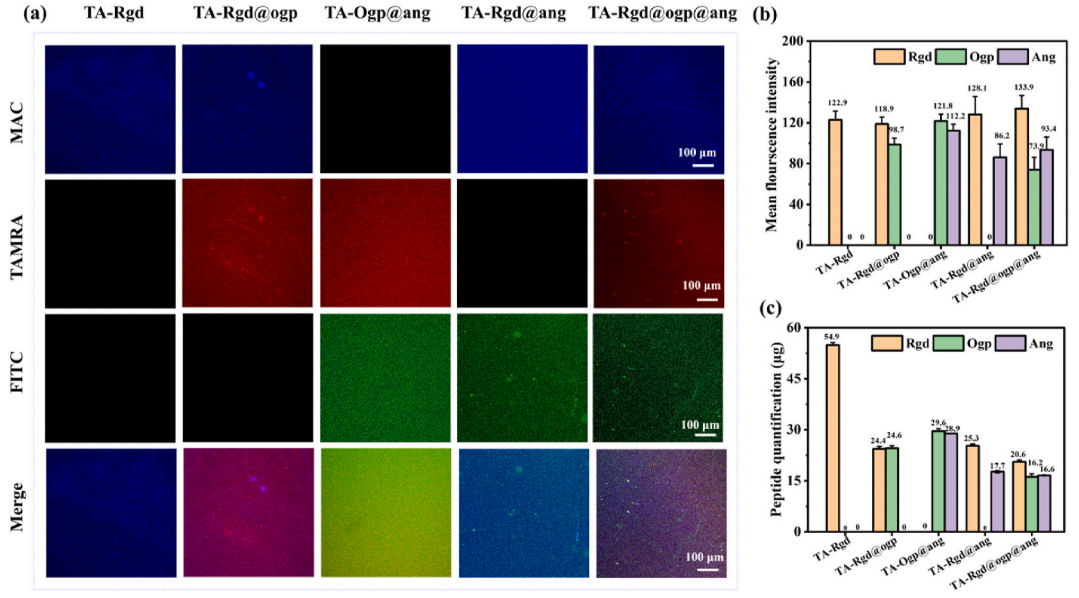

Fig. 3. Quantification of peptide content on the mixed peptide–decorated glass surfaces via fluorescent labeling. (a) Visualization of fluorescently labeled peptides (MCA-Rgd, TAMRA-Ogp and FITC-Ang) immobilized onto glass substrates. (b) The average fluorescence intensity of the peptides-decorated substrates. (c) Determination of polypeptide content with different substrates.

species. There were no significant differences observed among the TA-Rgd, TA-Rgd@ogp, TA-Ogp@ang, TA-Rgd@ang, and TA-Rgd@ogp@ang groups.

3.4. Promoting osteoblast migration, early adhesion, and proliferation in vitro

The cell scratch assay is a commonly used method to demonstrate cell migration ability. In Fig. 4a, it can be observed that after 24 h of migration, the migration area of the coatings modified with various peptides and the control group all showed significant increases. The statistical results in Fig. 4d show that the migration area proportion of the blank group is 15 %, TA-Rgd is 52%, and TA-Rgd@ogp@ang reaches 59 %. The proportions of the other groups are around 50 %. It can be inferred that peptide coatings can effectively promote cell migration, with TA-Rgd@ogp@ang coating showing the best performance.

To investigate the role of coating surface in inducing cell adhesion behavior, the number of cells and images of cell cytoskeleton were observed using inverted microscopy at 2 h and 4 h, as shown in Fig. 4b. At 2 h, in the blank control, there were slightly fewer cells, with cells presenting a round shape and lacking cell extensions. In contrast, in the experimental groups modified with peptide coatings, the number of cells increased significantly, and cell morphology gradually transitioned from round to polygonal, although the cytoskeleton did not fully extend around the periphery. Among them, cells on the TA-Rgd@ogp@ang coating interface exhibited the best spreading, with morphology similar to normal cells. At 4 h, the cytoskeleton of the control group gradually extended, while cells on interfaces modified with peptide coatings had completely spread out, establishing tight and extensive connections between cells. The statistical results of cell number and cell spreading area are presented in Fig. 4e and f, respectively, consistent with the observed results in the images. The TA-Rgd@ogp@ang coating interface mediated the best cell adhesion, consistent with the conclusions drawn from the migration experiments.Subsequently, the cells remaining on the coating surface, while experiencing centrifugal force, were employed to mimic the adhesive behavior of cells subjected to shear force. As shown in Fig. 4c, compared to the control group, the TA-Rgd coating maintained the original cell state under shear force. In Fig. 4g–i, statistical analysis of cell number, area, and cell viability revealed that, compared to the control, the other peptide coatings exhibited good shear resistance. To better illustrate cell proliferation on the coatings, two cell lines, osteoblasts (Fig. S6a) and endothelial cells (Fig. S6b), were selected. Cell viability was measured at any two time points (Figs. S6c–d), and visualization was achieved through live/dead staining. The results showed no significant difference between the coated materials and the control on the first or second day. However, on the third day, interfaces modified with peptide coatings significantly enhanced the proliferation of both cell lines compared to the control, with cell viability ranging between 1.5 and 2.5.

3.5. The peptide coatings enhanced migration, adhension and angiogenesis of HUVECs in vitro

To explore the vascularization and migration ability of implant surface coatings, endothelial cell migration area was observed after 24 h using a cell scratch assay, reflecting migration ability. In Fig. 5a, coatings modified with peptides all exhibited significant migration-promoting abilities. Statistical analysis in Fig. 5c revealed that the TA-Rgd coating had the best migration ability, with a migration rate of 60 %, while TA-Rgd@ogp, TA-Ogp@ang, TA-Rgd@ang, and TA-Rgd@ogp@ang showed significant differences compared to the control, with migration rates reaching 50 %. As shown in Fig. 5b, vascularization was observed after 6 h of cell growth. In the control group, scattered cell clusters were observed, with no obvious tubular structures. Only a few incomplete tubular branches were observed in TA-Rgd and TA-Rgd@ogp, while abundant and obvious tubular branches were present in TA-Ogp@ang, TA-Rgd@ang, and TA-Rgd@ogp@ang. Statistical analysis (Fig. 5d–h) revealed significant differences in total branch length, branch number, and number of tubes containing Ang materials compared to the control, with TA-Rgd@ogp@ang showing the best effect followed by TA-Rgd@ang. Subsequently, the adhesion ability of HUVEC cells was further observed (Fig. 6a). At 2 h, compared to the control group, cells on the peptide-modified coatings exhibited clear vascular structures and extensive cell-cell communication. Statistical analysis of cell number (Fig. 6c) and cell area (Fig. 6d) from the images showed significant differences in all four groups of coatings compared to the control, with more cells and larger spreading areas observed, except for TA-Ogp@ang.

To further explore the expression of angiogenesis-related factors on the coating surface, as shown in Fig. 6b, the immunofluorescence staining of endothelial adhesion molecule CD31 revealed similar cell adhesion patterns. It can be observed that TA-Rgd@ang and TA-Rgd@ogp@ang exhibited abundant green fluorescence surrounding the cells, indicating high expression of CD31. As shown in Fig. 6e, statistical analysis of CD31 immunofluorescence revealed significant differences between TA-Ogp@ang and the control group, which was slightly lower than TA-Rgd@ang and TA-Rgd@ogp@ang. Subsequently, in Fig. 6f and g, the gene expression levels of VEGF and CD31 were quantitatively analyzed, with TA-Rgd@ogp@ang showing the highest expression levels for both factors.

3.6. Promotion of osteogenesis and mineralization of bone marrow mesenchymal stem cells in vitro

To investigate the functionality of coating materials in osteogenic differentiation and mineralization, the alkaline phosphatase (ALP) activity, Alizarin Red S (ARS) mineralization, and expression of osteogenic-specific marker genes were evaluated. Firstly, ALP activity peaked on day 4 and gradually decreased thereafter (Fig. 7a–b). By day 14, extracellular matrix mineralization was evident, with larger and more intense red nodules observed (Fig. 7c–d). The results indicate that coatings containing osteogenic peptides, such as Ogp, exerted a more pronounced osteogenic induction effect on bone marrow mesenchymal stem cells (BMSCs). Among them, the TA-Rgd@ogp@ang coating exhibited the best effect. Furthermore, quantitative reverse transcription-polymerase chain reaction (qRT-PCR) was performed to investigate the expression of osteogenic marker genes including osteocalcin (OCN), RUNX2, ALP, and type I collagen (COL-I) (Fig. 7e–h). The results revealed that, except for RUNX2, the expression levels of the other genes were consistent with the staining data mentioned above, indicating that coatings containing Ogp osteogenic peptides exhibited the highest expression levels, with TA-Rgd@ogp@ang demonstrating the most favorable effect.

3.7. Construction and repair of osteoporotic bone defects

The in *vitro* results indicate that mixed peptide coatings are beneficial for osteogenic differentiation and angiogenesis. To further investigate the bone integration of implant surface coating materials in osteoporotic bone defects, an osteoporotic rat (OVX) bone defect model was established. Figs. S8a–c show micro-computed tomography (μ-CT) images of the distal femoral metaphysis bone trabeculae three months after modeling in both the OVX and sham surgery (Sham) groups. The Sham group exhibited normal bone tissue structure, while the OVX group showed significantly disrupted bone trabecular structure and obvious bone loss. Additionally, the OVX group had significantly decreased bone volume/total volume (BV/TV), trabecular number (Tb.N), and connectivity density (Conn.D), while trabecular spacing (Tb.Sp) was significantly increased, and trabecular thickness (Tb.Th) showed no significant difference, indicating the successful establishment of the osteoporotic model (Fig. 8d). Subsequently, surgery was performed to implant bone defects in the distal femur, and the experiment was terminated after 8

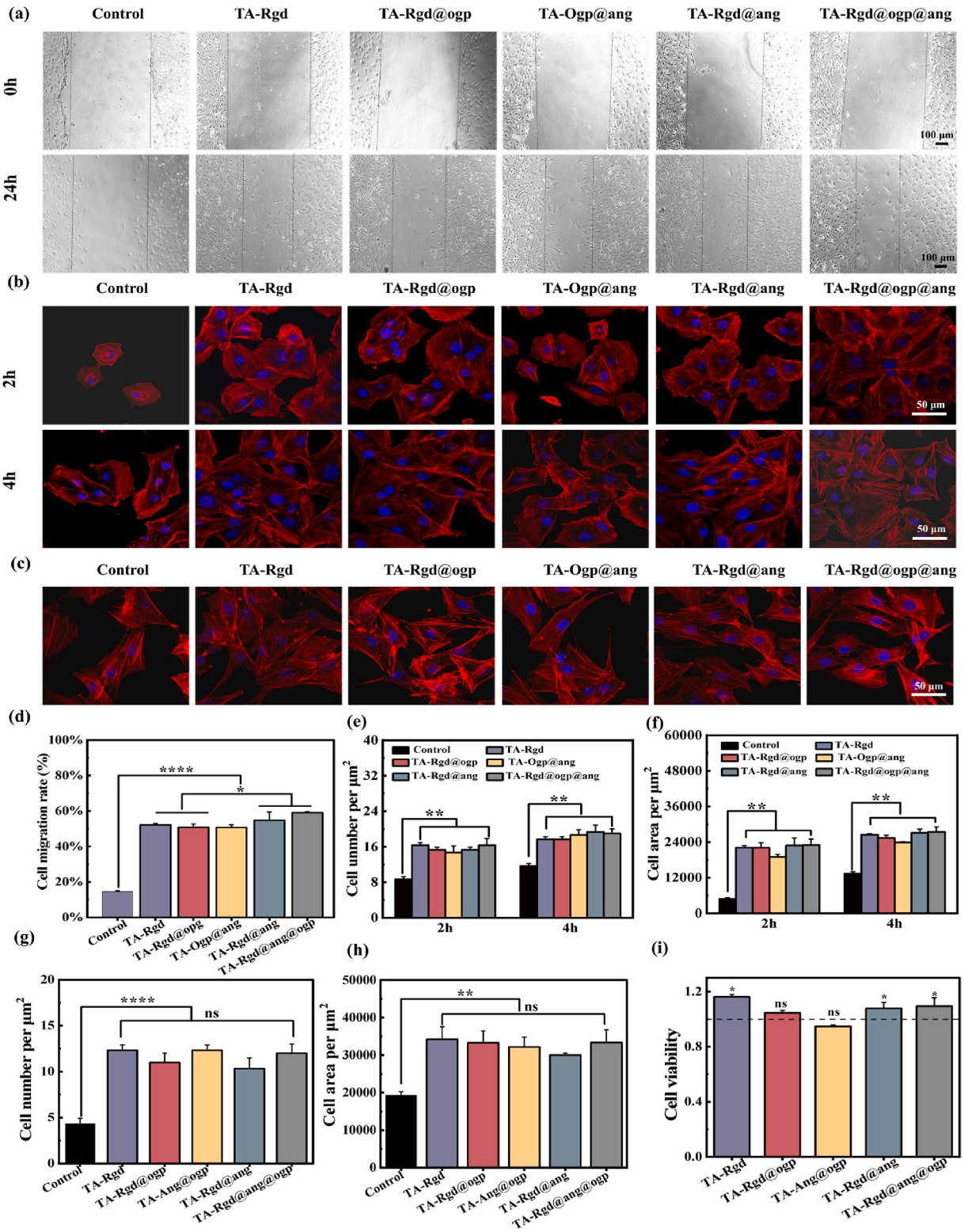

Fig. 4. (a) MC3T3-E1 cell migration on different coatings for 0 and 24 h, respectively. (b) Fluorescence microscope images of MC3T3-E1 cells seeded on different coatings for 2 and 4 h. (c) Fluorescence microscope images of cell adhesion under shear force. (d) Quantitative analysis of cell mobility in (a). (e) Number of MC3T3-E1 cells per μm^2 on different coatings. (f) Cell area of MC3T3-E1 cells per μm^2 on different coatings. (g) The number of nuclei of cells cultured on coating under shear force. (h) Cell area of MC3T3-E1 cells per μm^2 on different coatings under shear force. (i) Cell vibility of MC3T3-E1 cells on different coatings under shear force (difference analysis and results are compared with glass in the same period).

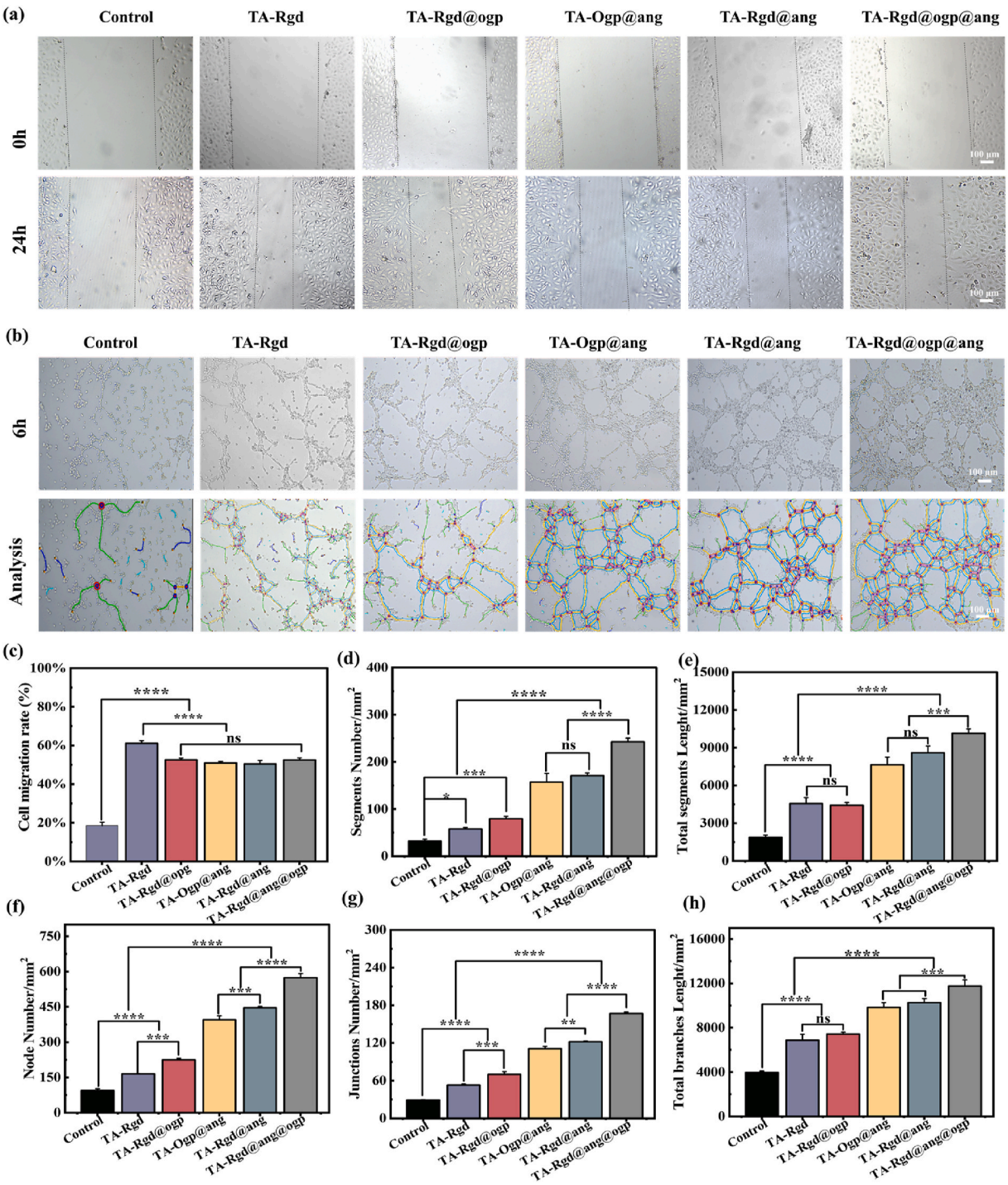

Fig. 5. (a) HUVEC cell migration on different coatings for 0 and 24 h, respectively. (b) The wound healing assay was performed to evaluate the effects of peptide composite on the migration ability of HUVEC. (c) Quantitative analysis of cell mobility in (a). (d–h) Tubular networking assessed in terms of number of segments, total segments lengtht, number of nodes, number of junctions, and total brunch length.

weeks of further feeding. The 3D models of the implants and surface neo-bone were constructed using CTVol (Fig. 8e). The results showed that, compared to the blank titanium rod, all five peptide-coated groups exhibited varying degrees of neo-bone formation. Among them, coatings carrying Ogp peptide, such as TA-Rgd@ogp, TA-Ogp@ang, and TA-Rgd@ogp@ang, showed abundant dense neo-bone formation on the surface. In contrast, the neo-bone formation area of TA-Rgd and TA-Rgd@ang was smaller. BV/TV, Tb.Th, Tb.N, and Tb.Sp data were obtained from μ-CT (Fig. 8f–i). The bone volume fraction of TA-Rgd@ogp@ang was the highest at 21 %, followed by TA-Rgd@ogp and TA-Ogp@ang coatings at 18.7 % and 18.2 %, respectively.

3.8. The histological and morphometric evaluation in vivo

Further analysis of the formation of new bone around different implants was conducted using HE, Masson's trichrome, and toluidine blue staining. HE staining images (Fig. 9a) revealed that compared to the control group, the implants covered with peptide coatings had a continuous and smooth contact surface with the new bone, indicating good healing (especially TA-Rgd@ogp and TA-Rgd@ogp@ang). Similar

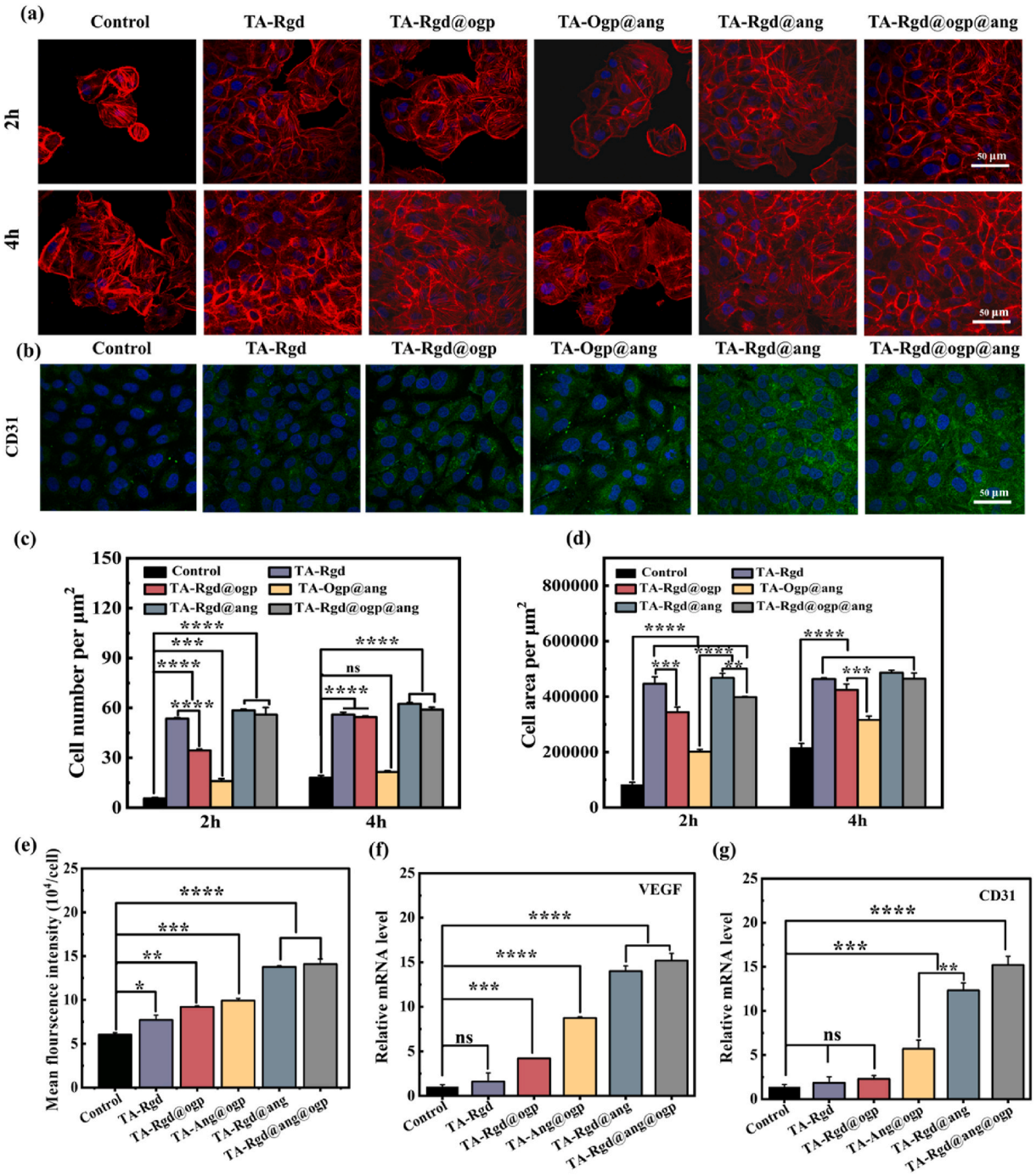

Fig. 6. (a) Fluorescence microscope images of HUVEC cells seeded on different coatings for 2 and 4 h. (b) Fluorescence microscope images of CD31 in HUVEC cells on different coating surfaces. (c) Number of HUVEC cells per μm^2 on different coatings. (d) Cell area of HUVEC cells per μm^2 on different coatings. (e) Mean CD31 immunofluorescence intensity was shown. mRNA expression levels of differentiation-related proteins (f) VEGF, (g) CD31 after culturing HUVEC cells on different coatings at 7 days.

results were observed in the Masson's trichrome staining images (Fig. 9b). As the colors in Masson's staining change gradually with bone maturation (from blue to red), we concluded that the new bone formation in the TA-Rgd@ogp and TA-Rgd@ogp@ang groups was more mature compared to that in the TA-Ogp@ang group. Toluidine blue staining is essential for evaluating the bone integration interface. As shown in Fig. S8, there was more new bone formation in the TA-Rgd@ogp and TA-Rgd@ogp@ang groups, with a continuous bone integration interface (blue lines) and a larger contact area.

To investigate the phenotypes of osteogenesis and angiogenesis around different implants in *vivo*, immunohistochemical staining was performed to detect OCN (yellow, a marker for bone mineralization) and CD31 (yellow, a marker for blood vessel formation). As shown in Fig. 9c, compared to the control, the expression of OCN (orange circles) was higher in the TA-Ogp@ang and TA-Rgd@ogp@ang coatings, with the latter showing more pronounced expression. As depicted in Fig. 9d, the expression of CD31 was significantly increased in the TA-Rgd@ang and TA-Rgd@ogp@ang coatings (orange arrows). In summary, the TA-Rgd@ogp@ang coating exhibited favorable effects on both angiogenesis and osteogenesis.

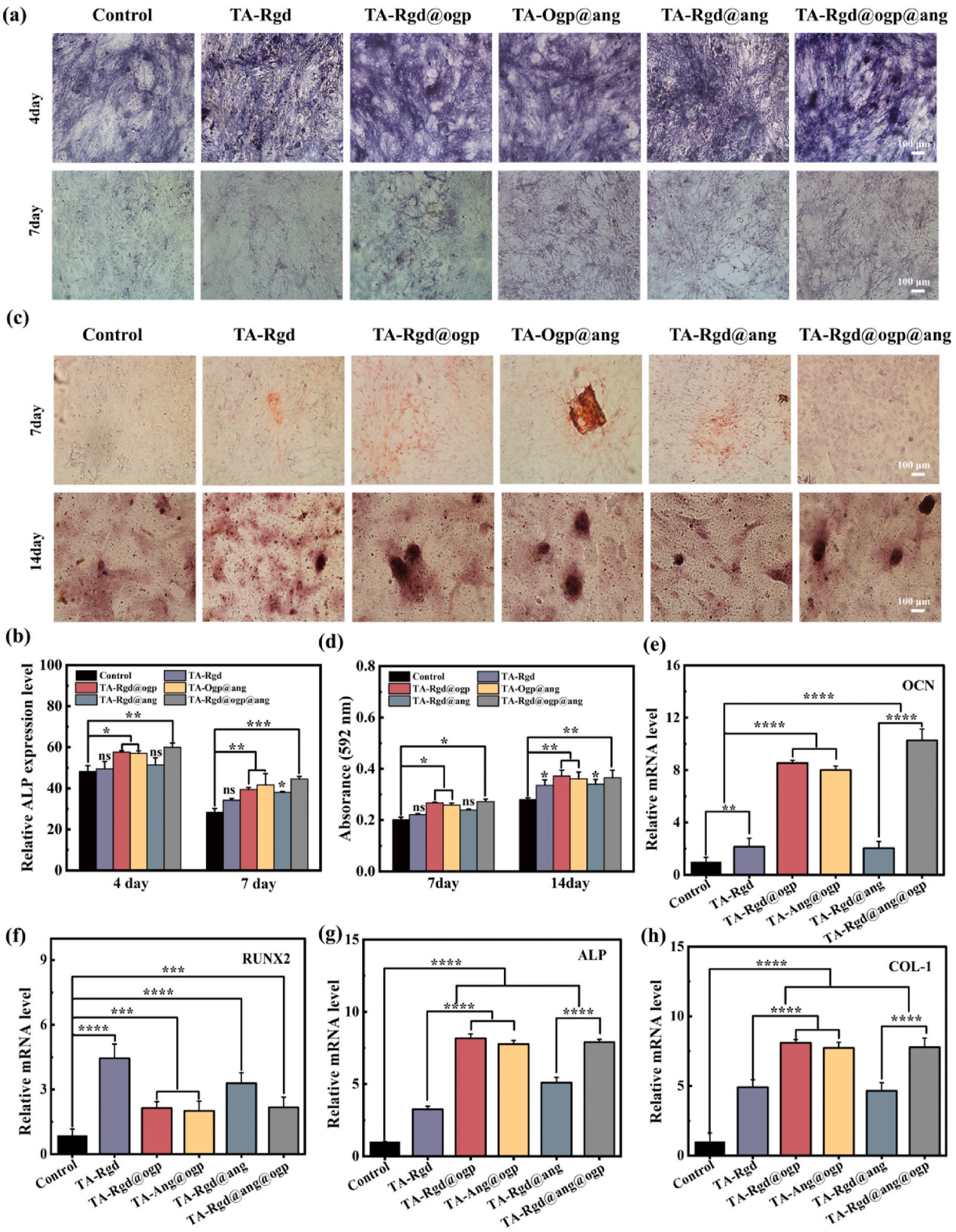

Fig. 7. Osteogenic staining analysis: (a) BMSCs cells were seeded on different peptide coatings and stained for ALP on days 4 and 7. (b) ALP activity quantification assay. (c) BMSCs cells were cultured on different coatings and stained for ARS on 7 and 14 days. (d) Quantification of alizarin red S staining; mRNA expression levels of differentiation-related proteins (e) OCN, (f) RUNX2, (g) ALP, and (h) COL-1 after culturing BMSCs cells on different coatings at 7 days. (For interpretation of the references to color in this figure legend, the reader is referred to the Web version of this article.)

4. Discussion

Patients with osteoporosis face difficulties such as decreased cell recruitment ability, reduced bone density, weakened osteogenic capacity, and decreased bone vascularization function, which leads to a higher failure rate of pure titanium implants and poor bone integration [30,31]. In the past decade, the design of biomolecule coatings on titanium-based materials to confer multifunctionality to the titanium

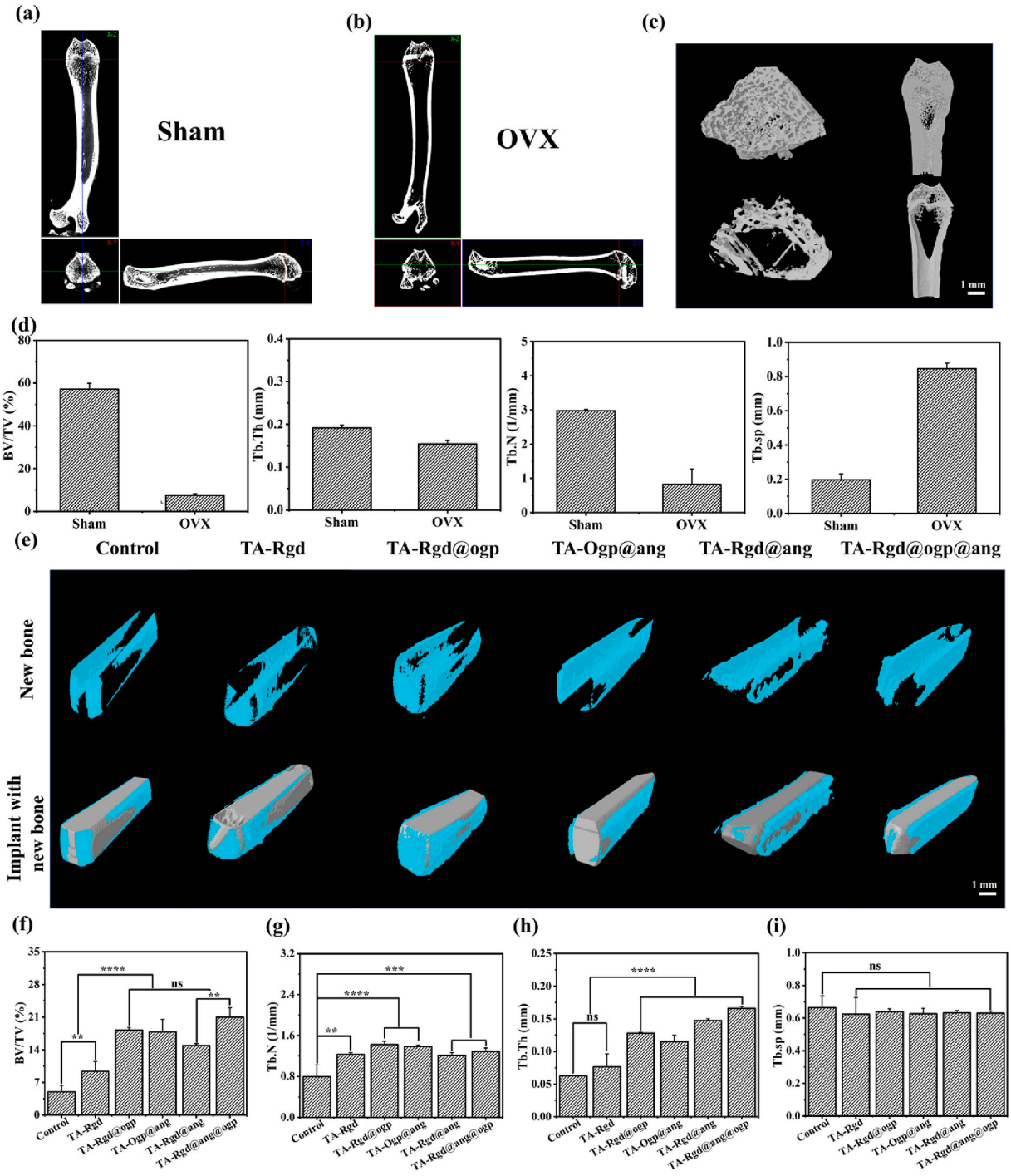

Fig. 8. The microcomputed tomography of sham surgery rat (a) and ovariectomy rat (b). (c) 3D image of sham and ovariectomy rat. (d) Quantitative analysis of bone volume/total volume (BV/TV), trabecular number (Tb.Th), trabecular thickness (Tb.N), and trabecular separation (Tb.Sp) of the femur in Sham and OVX rats 8 weeks after surgical castration. (e) Representative 3D reconstruction images of new bone. (f–i) Quantitative results of BV/TV (Bone volume fraction), Tb. N (Trabecular number), Tb. Th (Trabecular Thickness), and Tb.Sp (Trabecular separation).

surface for improving poor bone integration has been widely applied [32–36]. Here, we report a multifunctional interface strategy that can rationalize and optimize cell migration and adhesion, bone inductiveness, bone vascularization, and other functions onto titanium implants through simple LbL assembly.

Preliminary experimental exploration by our research group showed that under pH 7 conditions, both TA and K_6-peptide exhibited a linear growth trend when mixed at a 1:1 ratio (c1:c2) of polypeptides with the same linker [24]. Under this experimental condition, we synthesized a series of peptide coatings: TA-Rgd, TA-Rgd@ogp, TA-Ogp@ang, TA-Rgd@ang, and TA-Rgd@ogp@ang. Through combined analysis using ellipsometric spectroscopy and quartz crystal microbalance with dissipation (QCM-D), changes in coating thickness and mass during LbL deposition were accurately understood. Ellipsometric spectroscopy is a commonly used optical technique to characterize the properties of thin films at interfaces, and appropriate data processing can obtain quantitative information such as the thickness and quality of films at interfaces [37]. QCM-D measurements with dissipation monitoring capability are

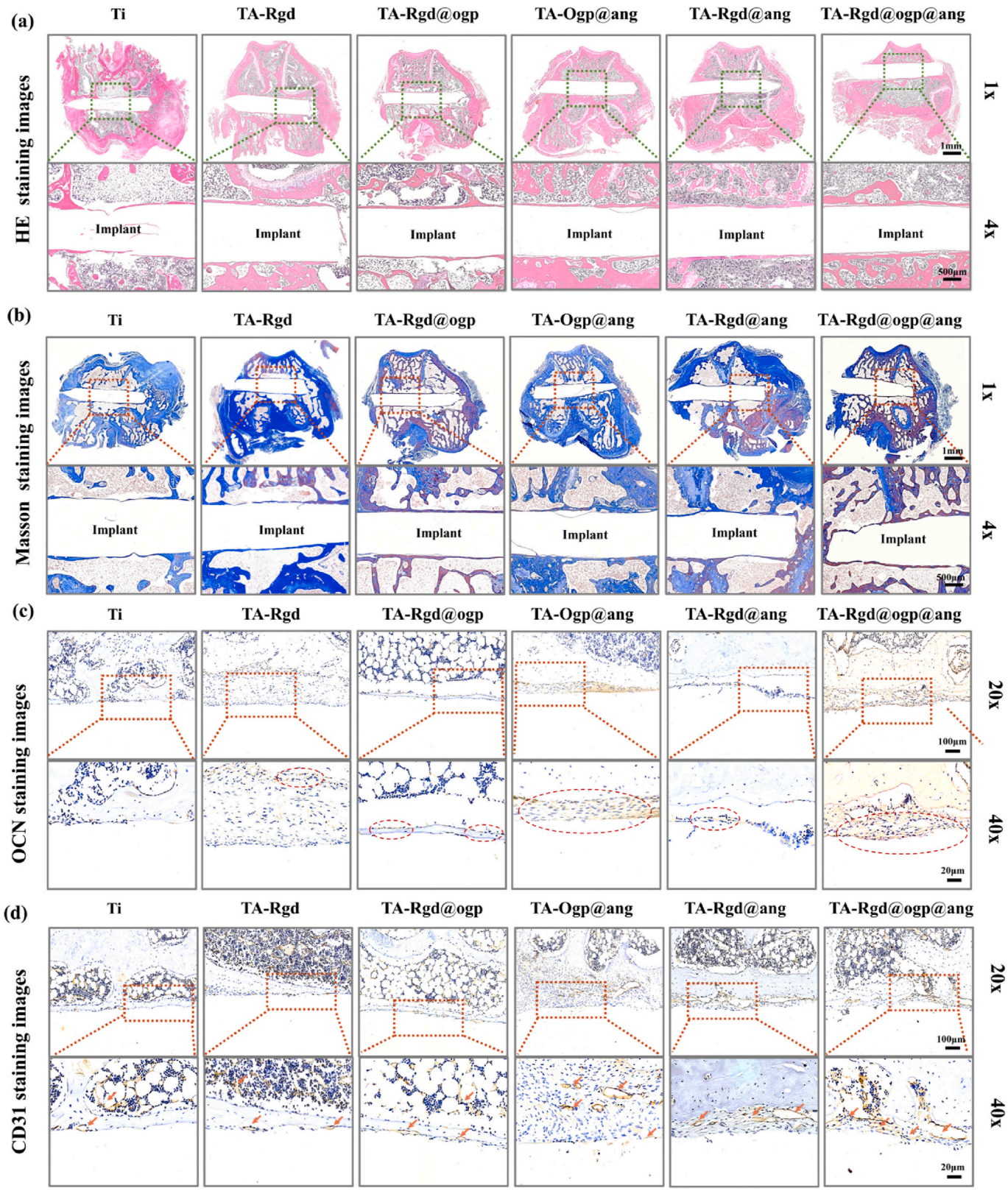

Fig. 9. Evaluation of new bone formation and maturation in *vivo*: (a) Representative HE staining images of surrounding bone tissue for different implants. (b) Representative Masson staining images of new bone maturation around different implants. Blue and red represent low and high maturity of bone tissue, respectively. (c) Immunohistochemical evaluation of osteogenic factor OCN expression, with red circles indicating osteogenic expression locations. (d) Immunohistochemical evaluation of vascular factor CD31 expression, with orange arrows indicating CD31-positive vessels. (For interpretation of the references to color in this figure legend, the reader is referred to the Web version of this article.)

highly sensitive to the quality of surface binding layers, with a resolution on the order of ng/cm^2 [38]. From the structure of the Rgd peptide, it can be observed that compared to Ogp/Ang peptides, Rgd is rich in arginine and possesses a large amount of positive charge, leading to a more pronounced interaction with TA, resulting in significantly higher thickness and adsorption mass of TA-Rgd coatings compared to other peptide coatings (Fig. 1a–f and Figs. S1a–c). This is consistent with the findings of Caruso et al. [39], indicating that positively charged peptides exhibit stronger interactions with polyphenols (K_a of 2×10^4 M^{-1}). The remaining peptide coatings show a certain degree of Rgd dependence, with slightly higher thickness when Rgd peptides are present in the coating composition, but with no significant differences. It can be inferred that, excluding the interference of Rgd carrying charges, coatings of mixed peptides TA-Rgd@ogp, TA-Ogp@ang, TA-Rgd@ang, and TA-Rgd@ogp@ang at the same k_6 junction demonstrate similar deposition rates. This approach avoids competitive relationships between two or three peptides simultaneously assembling with TA, preserving the spatial conformation and functionality of the peptides themselves.

In the material characterization tests, we selected a coating assembly of 10 layers (the minimum film thickness covering the substrate) for experimentation [24]. Hydrophilic surfaces of implants aid in wetting, adsorption, and substance transfer, facilitating rapid reaction with the moist blood environment of the wound, thereby accelerating bone integration and shortening the treatment cycle [40]. The contact angle of the peptide-modified coating interface significantly decreased compared to pure titanium, exhibiting excellent hydrophilicity (Fig. 1g), which is closely related to the hydrophilic amino acids in the peptides. TA contains multiple hydrophobic aromatic rings and hydrophilic phenolic hydroxyl groups, providing abundant reaction sites that can be involved in various dynamic covalent bonding, metal-organic coordination interactions, and non-covalent interactions [41]. To determine the primary forces between TA and peptides, XPS analysis showed only C–N bonds in the N peak, with no appearance of C═N double bonds (Fig. 1i), indicating that the binding force between TA and peptides is mainly non-covalent interactions, excluding covalent bonding. During AFM testing, surface properties changed under different environments, resulting in variations in the applied force and consequently changes in morphology and Young's modulus in gas and liquid phases (Fig. 2a and S3a). Peptides form adhesive layers in biological interfaces due to electrostatic, hydrogen bonding, and other interactions [42]. It can be assumed that the stronger the binding force between peptides and the interface, the stronger their adhesion and viscosity. This may be why the adhesion of TA-Rgd coatings in gas and liquid phases in AFM testing is slightly higher than that of other coatings (Fig. 2b–c and Figs. S3b–c). Additionally, exposure to a liquid environment leads to softer and more porous coating surfaces. Differences in adhesive capability may also result from differences in the hydration of peptide coatings, which are influenced by the testing environment (liquid or gas).

In normal tissues or cells, reactive oxygen species (ROS) are maintained in a dynamic equilibrium through biological elimination and generation. However, under non-physiological conditions such as trauma, inflammation, etc., the oxidative stress microenvironment becomes imbalanced, leading to the release of large amounts of ROS, which damages cell membranes and corresponding lipids, resulting in failed bone integration [43,44]. Therefore, the ability of implant surface coatings to eliminate reactive oxygen species is essential. The TA-Rgd, TA-Rgd@ogp, TA-Ogp@ang, TA-Rgd@ang, and TA-Rgd@ogp@ang groups all demonstrate significant ROS scavenging capabilities, with no significant differences among the groups (Fig. S5d). It can be inferred that TA plays a primary role in antioxidant activity within the coatings [45]. This is crucial for regulating the balance of the high ROS microenvironment in osteoporosis, which is a prerequisite for the coatings to exert important biological functions. Since the integration and long-term success of implants are determined by complex reactions occurring at the tissue-material interface, one of the most relevant issues in bone tissue engineering is the ability to reconstruct communication between autografts and the surrounding biological environment. Therefore, cell migration, adhesion, and proliferation are induced by coordinated transmembrane signals occurring in cells close to the implant surface, which are necessary for implant colonization. Cell adhesion is mainly achieved through two different mechanisms: (1) interactions between heparin binding sites on the extracellular matrix (ECM); (2) interactions of cell membrane heparan sulfate proteoglycans. In simple terms, it involves the recognition and interaction between integrin receptors and protein ligands in the ECM [46]. Xiao-Yu Yang et al. engineered crosslinked nanolayer interfaces using synthetic peptides synthesized from poly[LA-*co*-(Glc-*alt*-Lys)] and modified with Rgd and β-FGF molecules, which enhanced cell adhesion and differentiation [47]. Since the Rgd peptide motif interacts extensively with cell membrane integrins, coatings containing Rgd peptides exhibit higher cell migration and adhesion compared to other mixed peptide coatings (Fig. 4d–f and Fig. 5c). Furthermore, the TA-Rgd@ogp@ang coating showed the highest cell migration rate, indicating that the peptide activity was not lost, and there was a certain synergy among the three peptides, consistent with the conclusions from material characterization validation, that there was no competition between the various peptide groups. The adhesive force at the interface of the TA-Ogp@ang coating was slightly lower, possibly due to the negative polarity of the material interface [22]. Moreover, with the joint verification of osteoblasts and endothelial cells, it can be inferred that the universality of coating materials in promoting cell migration abilities can be applied to other medical fields.

The vascular system serves as a crucial conduit for the transportation of nutrients, oxygen, hormones, growth factors, and neurotransmitters, which are indispensable for bone regeneration and remodeling [48–50]. Recent studies have indicated that the bone integration process in osteoporosis involves not only the structural reconstruction of bone absorption and bone formation but also vascular regeneration, which constitutes an important part of the entire process [51,52]. HUVECs can retain their rapid proliferation characteristics on matrix gel, providing a good simulation of in *vitro* angiogenesis. Both matrix gel experiments and immunofluorescence staining of CD31 (an endothelial adhesion molecule distributed at tight junctions between endothelial cells, involved in vascular genesis [53]) have demonstrated that the TA-Rgd@ogp@ang promotes the best vascularization effect (Figs. 5b and 6b), fully illustrating that the Ang peptide retains its original vascularization function when bound to the coating, and its function is complemented by the Rgd and Ogp peptides. As an early marker of osteogenic activity [54], the early activity of ALP (at 4 days) provides sufficient evidence for the excellent differentiation-inducing ability of the Ogp peptide on BMSC cells (Fig. 7a). Combined with the mineralization characterization of late-stage osteogenesis using ARS staining (Fig. 7b), the synergistic effect of the mixed peptide coating TA-Rgd@ogp@ang on bone healing is demonstrated.

After demonstrating the excellent cell migration and adhesion capability, osteogenic properties, and bone vascularization potential of the TA-Rgd@ogp@ang implant coating in *vitro*, we further investigated the bone integration ability of the implant through in *vivo* studies. In this study, we performed bilateral ovariectomy (OVX) on rats to establish an osteoporosis model (Fig. 8a–d). All results from micro-CT, HE, Masson (Fig. 8e–i and Fig. 9a–b), and toluidine blue staining (Fig. S8) confirm that the TA-Rgd@ogp@ang coating is most conducive to new bone formation and bone integration around the implant. Immunohistochemical staining observations (Fig. 9c–d) revealed a significant increase in osteogenic markers (OCN) in both TA-Rgd@ogp@ang and TA-Rgd@ogp coatings, and a significant increase in vascular markers (CD31) in TA-Rgd@ogp@ang and TA-Rgd@ang coatings. In summary, the TA-Rgd@ogp@ang coating combines the advantages of Ogp osteogenic peptide and Ang angiogenic peptide, promoting osteogenesis and bone vascularization, consistent with our in *vitro* experimental results.

The toxicological evaluation of medical materials is particularly important. Based on existing research reports, the coating is composed

of relatively safe polyphenols and peptides. Secondly, the coating is applied in an amount of approximately nanograms, and stability tests further prove that the coating itself is stable and unlikely to have significant release. Finally, in vitro experiments using CCK8 and live/dead staining have shown that the toxicity of the coating is very low. Therefore, we believe that it will not have a significant impact on future practical applications. However, before actual application, it must undergo a series of standardized toxicity evaluations.

In conclusion, our multifunctional molecular coating strategy combines the polyphenolic peptide network (TA-K_6-peptide) with layer-by-layer assembly technology to rationally integrate and optimize cell migration and adhesion, osteoinductivity, and bone vascularization onto titanium implants. Besides offering desirable biological functionalities, the layer-by-layer assembly approach provides a slower and more enduring effect, as physically adsorbed peptides are prone to desorb from the implant surface and rapidly lose activity in the free state. Conversely, peptides covalently grafted tend to exhibit short-term burst release, thereby compromising their biological functionalities. Furthermore, this strategy offers advantages such as ease of operation, mild experimental conditions, and uniform modification of irregularly shaped implants. The hydrophilicity of the titanium surface is increased after modification with active peptides, which aids in enhancing cell compatibility. Additionally, the interaction between the common junction K_6 and the polyphenolic interface enables the realization of several peptides without interference, thereby collectively exerting effects. Therefore, in our study, achieving bone integration of titanium implants in osteoporotic environments can be easily accomplished. This also provides a universal and feasible approach to achieving various persistent biological functionalities on biomaterials, thus holding significant promise for future medical devices.

5. Conclusion

In summary, this study successfully fabricated a biofunctional TA-Rgd@ogp@ang composite coating with excellent mechanical and adhesive properties, as well as layer-by-layer sustained release capability, and applied it to titanium implants to improve osseointegration under osteoporotic conditions. The TA-Rgd@ogp@ang composite coating modulates the high ROS microenvironment of the bone marrow to maintain bone homeostasis, promoting osteogenic function of MC3T3-E1 and BMSCs. Additionally, it induces endothelial cell angiogenesis, facilitating the transportation of nutrients, oxygen, hormones, growth factors, and neurotransmitters, and it effectively exerts a triple effect of cell migration and adhesion, osteogenesis stimulation, and angiogenesis promotion under osteoporotic pathological conditions. This effectively addresses the issue of poor osseointegration of implants under osteoporotic pathological conditions.

CRediT authorship contribution statement

Jiming Liu: Writing – original draft, Visualization, Methodology, Investigation, Data curation. **Bingyang Zhao:** Writing – original draft, Visualization, Investigation. **Xinkun Shen:** Visualization, Investigation. **Dandan Lu:** Software, Methodology. **Wei he:** Validation, Software. **Xingjie Zan:** Visualization, Investigation. **Lianxin Li:** Supervision, Conceptualization. **Yihuai Pan:** Writing – original draft, Supervision, Conceptualization.

Declaration of competing interest

The authors declare that they have no known competing financial interests or personal relationships that could have appeared to influence the work reported in this paper.

Data availability

Data will be made available on request.

Acknowledgment

This work was supported by Wenzhou Science and Technology Bureau Industrial Science and Technology Project (Y20210119). Drawing material is from Home for Researchers (www.home-for-researchers.com).

Appendix A. Supplementary data

Supplementary data to this article can be found online at https://doi.org/10.1016/j.mtbio.2024.101150.

References

[1] F. Ordikhani, A. Simchi, Long-term antibiotic delivery by ChitosanBased composite coatings with bone regenerative potential, Appl. Surf. Sci. 317 (2014) 56–66, https://doi.org/10.1016/j.apsusc.2014.07.197.
[2] X. Lu, Z. Wu, K. Xu, X. Wang, S. Wang, H. Qiu, X. Li, J. Chen, Multifunctional coatings of titanium implants toward promoting osseointegration and preventing infection: recent developments, Front. Bioeng. Biotechnol. 9 (2021) 783816, https://doi.org/10.3389/fbioe.2021.783816.
[3] S. Xu, G. Tian, M. Zhi, Z. Liu, Y. Du, X. Lu, M. Li, J. Bai, X. Li, J. Deng, S. Ma, Y. Wang, ACS Biomater. Sci. Eng. 4 (2024) 2463–2476, https://doi.org/10.1021/acsbiomaterials.3c01858.
[4] Y. Zhou, Y. Deng, Z. Liu, M. Yin, M. Hou, Z. Zhao, X. Zhou, L. Yin, Cytokine-scavenging nanodecoys reconstruct osteoclast/osteoblast balance toward the treatment of postmenopausal osteoporosis, Sci. Adv. 7 (2021) eabl6432, https://doi.org/10.1126/sciadv.abl6432.
[5] Y. Zhao, H. Kang, X. Wu, P. Zhuang, R. Tu, T. Goto, F. Li, H. Dai, Multifunctional scaffold for osteoporotic pathophysiological microenvironment improvement and vascularized bone defect regeneration, Adv. Healthcare Mater. 12 (2023) 2203099, https://doi.org/10.1002/adhm.202203099.
[6] G. Manzano, J. Montero, J. Martín-Vallejo, Fabbro M. Del, M. Bravo, T. Testori, Risk Factors in Early Implant Failure: a Meta-Analysis Implant Dentistry, vol. 25, 2016, pp. 272–280, https://doi.org/10.1097/ID.0000000000000386.
[7] S.R. Cummings, L.J. Melton, Epidemiology and outcomes of osteoporotic fractures, Lancet 359 (2002) 1761–1767, https://doi.org/10.1016/S0140-6736(02)08657-9.
[8] R.M. Neer, C.D. Arnaud, J.R. Zanchetta, R. Prince, G.A. Gaich, J.Y. Reginster, A. B. Hodsman, E.F. Eriksen, S. IshmShalom, H.K. Genant, O. Wang, B.H. Mitlak, Effect of parathyroid hormone (1-34) on fractures and bone mineral density in postmenopausal women with osteoporosis, N. Engl. J. Med. 344 (2001) 1434–1441, https://doi.org/10.1056/NEJM200105103441904.
[9] L.J. Melton, E.A. Chrischilles, C. Cooper, A.W. Lane, B.L. Riggs, How many women have osteoporosis? JBMR Anniversary Classic, J. Bone Miner. Res. 20 (2005) 886–892, https://doi.org/10.1359/jbmr.2005.20.5.886.
[10] J.A. Kanis, Diagnosis of osteoporosis and assessment of fracture risk, Lancet 359 (2002) 1929–1936, https://doi.org/10.1016/S0140-6736(02)08761-5.
[11] C. Lei, J. Song, S. Li, Y. Zhu, M. Liu, M. Wan, Z. Mu, F.R. Tay, L. Niu, Advances in materials-based therapeutic strategies against osteoporosis, Biomaterials 296 (2023) 122066, https://doi.org/10.1016/j.biomaterials.2023.122066.
[12] P. Jiang, Y. Zhang, R. Hu, B. Shi, L. Zhang, Q. Huang, Y. Yang, P. Tang, C. Lin, Advanced surface engineering of titanium materials for biomedical applications: from static modification to Dynamic responsive regulation, Bioact. Mater. 27 (9) (2023) 15–57, https://doi.org/10.1016/j.bioactmat.2023.03.006.
[13] S. He, C. Duan, S. Wang, Y. Yu, Y.K. Chan, X. Shi, J. Huang, S. Wang, S. Peng, Y. Deng, Fusion peptide-engineered polyetheretherketone implants with photo-assisted anti-pathogen and enhanced angiogenesis for in *vivo* osseointegrative fixation, Chem. Eng. J. 446 (2022) 137453, https://doi.org/10.1016/j.cej.2022.137453.
[14] K. Aoki, N. Alles, N. Soysa, K. Ohya, Peptide-based delivery to bone, Adv. Drug Deliv. Rev. 64 (2012) 1220–1238, https://doi.org/10.1016/j.addr.2012.05.017.
[15] B. Wang, A. Bian, F. Jia, J. Lan, H. Yang, K. Yan, L. Xie, H. Qiao, X. Chang, H. Lin, H. Zhang, Y. Huang, "Dual-functional" strontium titanate nanotubes designed based on fusion peptides simultaneously enhancing anti-infection and osseointegration, Biomater. Adv. 133 (2022) 112650, https://doi.org/10.1016/j.msec.2022.112650.
[16] B. Wang, J. Lan, H. Qiao, L. Xie, H. Yang, H. Lin, X. Li, Y. Huang, Porous surface with fusion peptides embedded in strontium titanate nanotubes elevates osteogenic and antibacterial activity of additively manufactured titanium alloy, Colloids Surf. B Biointerfaces 224 (2023) 113188, https://doi.org/10.1016/j.colsurfb.2023.113188.
[17] J. Bai, G. Ge, Q. Wang, W. Li, K. Zheng, Y. Xu, H. Yang, G. Pan, D. Geng, Engineering stem cell recruitment and osteoinduction via bioadhesive molecular mimics to improve osteoporotic bone-implant integration, Research 14 (2022) 9823784, https://doi.org/10.34133/2022/9823784.

[18] R.R. Costa, J.F. Mano, Polyelectrolyte multilayered assemblies in biomedical Technologies, Chem. Soc. Rev. 43 (2014) 3453–3479, https://doi.org/10.1039/C3CS60393H.
[19] J.J. Richardson, J. Cui, M. Bjornmalm, J.A. Braunger, H. Ejima, F. Caruso, Innovation in layer-by-layer assembly, Chem. Rev. 116 (2016) 14828–14867, https://doi.org/10.1021/acs.chemrev.6b00627.
[20] J.J. Richardson, M. Bjornmalm, F. Caruso, Technology-driven layer-by-layer assembly of nanofilms, Science 348 (2015) aaa2491, https://doi.org/10.1126/science.aaa2491.
[21] S.A. Abouelmagd, F. Meng, B.K. Kim, H. Hyun, Y. Yeo, Tannic acid-mediated surface functionalization of polymeric nanoparticles, ACS Biomater. Sci. Eng. 2 (2016) 2294–2303, https://doi.org/10.1021/acsbiomaterials.6b00497.
[22] H.S. Liang, Y.Q. Pei, J. Li, W.F. Xiong, Y. He, S.L. Liu, Y. Li, B. Li, pH-Degradable antioxidant nanoparticles based on hydrogen-bonded tannic acid assembly, RSC Adv. 6 (2016) 31374–31385, https://doi.org/10.1039/C6RA02527G.
[23] L.W. Yang, L.L. Han, Q. Liu, Y.G. Xu, L.Y. Jia, Galloyl groups-regulated fibrinogen conformation: understanding antiplatelet adhesion on tannic acid coating, Acta Biomater. 64 (2017) 187–199, https://doi.org/10.1016/j.actbio.2017.09.034.
[24] B. Zhao, Y. Dong, X. Shen, W. He, H. Jin, L. Yao, S. Zheng, X. Zan, J. Liu, Construction of multifunctional coating with cationic amino acid-coupled peptides for osseointegration of implants, Materials Today Bio 23 (2023) 100848, https://doi.org/10.1016/j.mtbio.2023.100848.
[25] L. Padiolleau, C. Chanseau, S. Durrieu, C. Ayela, G. Laroche, M.C. Durrieu, Directing hMSCs fate through geometrical cues and mimetics peptides, J. Biomed. Mater. Res. 108 (2020) 201–211, https://doi.org/10.1002/jbm.a.36804.
[26] M. Yakufu, Z. Wang, Y. Wang, Z. Jiao, M. Guo, J. Liu, P. Zhang, Covalently functionalized poly(etheretherketone) implants with osteogenic growth peptide (OGP) to improve osteogenesis activity, RSC Adv. 10 (2020) 9777–9785, https://doi.org/10.1039/D0RA00103A.
[27] Y.C. Chen, I. Bab, N. Mansur, M. Namdar-Attar, H. Gavish, M. Vidson, A. Muhlrad, A. Shteyer, M. Chorev, Structure–bioactivity of C-terminal pentapeptide of osteogenic growth peptide [OGP (10–14)], J. Pept. Res. 56 (2000) 147–156, https://doi.org/10.1034/j.1399-3011.2000.00763.x.
[28] Y. Hamada, H. Egusa, Y. Kaneda, I. Hirata, N. Kawaguchi, T. Hirao, T. Matsumoto, M. Yao, K. Daito, M. Suzuki, H. Yatani, Synthetic osteopontin-derived peptide SVVYGLR can induce neovascularization in artificial bone marrow scaffold biomaterials, Dent. Mater. J. 26 (2007) 487–492, https://doi.org/10.4012/dmj.26.487.
[29] H. Egusa, Y. Kaneda, Y. Akashi, Y. Hamada, T. Matsumoto, M. Saeki, D.K. Thakor, Y. Tabata, N. Matsuura, H. Yatani, Enhanced bone regeneration via multimodal actions of synthetic peptide SVVYGLR on osteoprogenitors and osteoclasts, Biomaterials 30 (2009) 4676–4686, https://doi.org/10.1016/j.biomaterials.2009.05.032.
[30] B. Yuan, L. Wang, R. Zhao, X. Yang, X. Yang, X. Zhu, L. Liu, K. Zhang, Y. Song, X. Zhang, A biomimetically hierarchical polyetherketoneketone scaffold for osteoporotic bone repair, Sci. Adv. 6 (2020) eabc4704, https://doi.org/10.1126/sciadv.abc4704.
[31] L. Mao, L. Xia, J. Chang, J. Liu, L. Jiang, C. Wu, B. Fang, The synergistic effects of Sr and Si bioactive ions on osteogenesis, osteoclastogenesis and angiogenesis for osteoporotic bone regeneration, Acta Biomater. 61 (2017) 217–232, https://doi.org/10.1016/j.actbio.2017.08.015.
[32] C. Wang, H. Hu, Z. Li, Y. Shen, Y. Xu, G. Zhang, X. Zeng, J. Deng, S. Zhao, T. Ren, Y. Zhang, Enhanced osseointegration of titanium alloy implants with laser microgrooved surfaces and graphene oxide coating, ACS Appl. Mater. Interfaces 11 (2019) 39470–39483, https://doi.org/10.1021/acsami.9b12733.
[33] M. Lai, K. Cai, L. Zhao, X. Chen, Y. Hou, Z. Yang, Surface functionalization of TiO2 nanotubes with bone morphogenetic protein 2 and its synergistic effect on the differentiation of mesenchymal stem cells, Biomacromolecules 12 (2011) 1097–1105, https://doi.org/10.1021/bm1014365.
[34] X. Shen, Y. Hu, G. Xu, W. Chen, K. Xu, Q. Ran, P. Ma, Y. Zhang, J. Li, K. Cai, Regulation of the biological functions of osteoblasts and bone formation by Zn-Incorporated coating on microrough titanium, ACS Appl. Mater. Interfaces 6 (2014) 16426–16440, https://doi.org/10.1021/am5049338.
[35] Y. He, K. Xu, K. Li, Z. Yuan, Y. Ding, M. Chen, C. Lin, B. Tao, X. Li, G. Zhang, P. Liu, K. Cai, Improved osteointegration by SEW2871-encapsulated multilayers on microstructured titanium via macrophages recruitment and immunomodulation, Appl. Mater. Today 20 (2020) 100673, https://doi.org/10.1016/j.apmt.2020.100673.
[36] F. Jia, D. Xu, Y. Sun, W. Jiang, H. Yang, A. Bian, Y. Liu, K. Liu, S. Zhang, Y. Wang, H. Qiao, H. Lin, J. Lan, Y. Huang, Strontium-calcium doped titanium dioxide nanotubes loaded with GL13K for promotion of antibacterial activity, anti-Inflammation, and vascularized bone regeneration, Ceram. Int. 22 (2023) 35703–35721, https://doi.org/10.1016/j.ceramint.2023.08.250.
[37] J.J.I. Ramos, I. Llarena, L. Fernandez, S.E. Moya, E. Donath, Controlled stripping of polyelectrolyte multilayers by quaternary ammonium surfactants, Macromol. Rapid Commun. 30 (2009) 1756–1761, https://doi.org/10.1002/marc.200900280.
[38] K. Haberska, T. Ruzgas, Polymer multilayer film formation studied by in situ ellipsometry and electrochemistry, Bioelectrochemistry 76 (2009) 153–161, https://doi.org/10.1016/j.bioelechem.2009.05.007.
[39] Y. Han, R.P.M. Lafleur, J. Zhou, W. Xu, Z. Lin, J.J. Richardson, F. Caruso, Role of molecular interactions in supramolecular polypeptide-polyphenol networks for engineering functional materials, J. Am. Chem. Soc. 27 (2022) 12510–12519, https://doi.org/10.1021/jacs.2c05052.
[40] L. Tang, P. Thevenot, W. Hu, Surface chemistry influences implant biocompatibility, Curr. Top. Med. Chem. 4 (2008) 270–280, https://doi.org/10.2174/156802608783790901.
[41] J. Zhou, Z. Lin, Y. Ju, M.A. Rahim, J.J. Richardson, F. Caruso, Polyphenol-mediated assembly for particle engineering, Accounts Chem. Res. 7 (2020) 1269–1278, https://doi.org/10.1021/acs.accounts.0c00150.
[42] C. Chen, H. Yang, X. Yang, Q. Ma, Tannic acid: a crosslinker leading to versatile functional polymeric networks: a review, RSC Adv. 13 (2022) 7689–7711, https://doi.org/10.1039/D1RA07657D.
[43] B. Chang, M. Zhang, G. Qing, T. Sun, Dynamic biointerfaces: from recognition to function, Small 11 (2015) 1097–1112, https://doi.org/10.1002/smll.201402038.
[44] V. Domazetovic, G. Marcucci, T. Iantomasi, M.L. Brandi, M.T. Vincenzini, Oxidative stress in bone remodeling: role of antioxidants, Clin. Cases Min. Bone Metab. 14 (2017) 209–216, https://doi.org/10.11138/ccmbm/2017.14.1.209.
[45] A. Baldwin, B.W. Booth, Biomedical applications of tannic acid, J. Biomater. Appl. 8 (2022) 1503–1523, https://doi.org/10.1177/08853282211058099.
[46] P. Brun, M. Scorzeto, S. Vassanelli, I. Castagliuolo, G. Palù, F. Ghezzo, et al., Mechanisms underlying the attachment and spreading of human osteoblasts: from transient interactions to focal adhesions on vitronectin-grafted bioactive surfaces, Acta Biomater. 4 (2013) 6105–6115, https://doi.org/10.1016/j.actbio.2012.12.018.
[47] N. Jiang, Y. Wang, X. Yin, P. Wei, L. Ying, B. Li, et al., bFGF and poly-RGD cooperatively establish biointerface for stem cell adhesion, proliferation, and differentiation, Adv. Mater. Interfac. 7 (2018) 1700702, https://doi.org/10.1002/admi.201700702.
[48] Joanna Filipowska, Krzysztof A. Tomaszewski, Łukasz Niedźwiedzki, Jerzy A. Walocha, Tadeusz Niedźwiedzki, The Role of Vasculature in Bone Development, Regeneration and Proper Systemic Functioning Angiogenesis, vol. 20, 2017, pp. 291–302, https://doi.org/10.1007/s10456-017-9541-1.
[49] Y. Zhuang, A. Liu, S. Jiang, U. Liaqat, K. Lin, W. Sun, C. Yuan, Promoting vascularized bone regeneration via strontium-incorporated hydroxyapatite bioceramic, Mater. Des. 234 (2023) 112313, https://doi.org/10.1016/j.matdes.2023.112313.
[50] J. Cui, X. Yu, B. Yu, X. Yang, Z. Fu, J. Wan, M. Zhu, X. Wang, K. Lin, Coaxially fabricated dual-drug loading electrospinning fibrous mat with programmed releasing behavior to boost vascularized bone regeneration, Adv. Healthcare Mater. 11 (2022) 2200571, https://doi.org/10.1002/adhm.202200571.
[51] G. Russow, D. Jahn, J. Appelt, S. Märdian, S. Tsitsilonis, J. Keller, Anabolic therapies in osteoporosis and bone regeneration, Int. J. Mol. Sci. 1 (2018) 83, https://doi.org/10.3390/ijms20010083.
[52] L.F. Cooper, Biologic determinants of bone formation for osseointegration: clues for future clinical improvements, J. Prosthet. Dent 4 (1998) 439–449, https://doi.org/10.1016/S0022-3913(98)70009-5.
[53] D. Feng, J.A. Nagy, K. Pyne, H.F. Dvorak, A.M. Dvorak, Ultrastructural localization of platelet endothelial cell adhesion molecule (PECAM-1, CD31) in vascular endothelium, J. Histochem. Cytochem. 1 (2004) 87–101, https://doi.org/10.1177/002215540405200109.
[54] C. Hoemann, H. El-Gabalawy, M.D. McKee, In vitro osteogenesis assays: influence of the primary cell source on alkaline phosphatase activity and mineralization, Pathol. Biol. 4 (2009) 318–323, https://doi.org/10.1016/j.patbio.2008.06.004.